nature communications

Article

https://doi.org/10.1038/s41467-025-56754-5

# Unraveling the molecular mechanism of polysaccharide lyases for efficient alginate degradation

Received: 15 January 2024

Accepted: 29 January 2025

Published online: 18 March 2025

Check for updates

José Pablo Rivas-Fernández[1], Marlene Vuillemin[2], Bo Pilgaard[2], Leesa J. Klau[3,8], Folmer Fredslund[4,9], Charlotte Lund-Hanssen[3], Ditte H. Welner[4], Anne S. Meyer[2], J. Preben Morth[2], Flora Meilleur[5,6], Finn L. Aachmann[3], Carme Rovira[1,7] ✉ & Casper Wilkens[2,10] ✉

Alginate lyases (ALs) catalyze the depolymerization of brown macroalgae alginates, widely used naturally occurring polysaccharides. Their molecular reaction mechanism remains elusive due to the lack of catalytically competent Michaelis-Menten-like complex structures. Here, we provide structural snapshots and dissect the mechanism of mannuronan-specific ALs from family 7 polysaccharide lyases (PL7), employing time-resolved NMR, X-ray, neutron crystallography, and QM/MM simulations. We reveal the protonation state of critical active site residues, enabling atomic-level analysis of the reaction coordinate. Our approach reveals an endolytic and asynchronous *syn* β-elimination reaction, with Tyr serving as both Brønsted base and acid, involving a carbanion-type transition state. This study not only reconciles previous structural and kinetic discrepancies, but also establishes a comprehensive PL reaction mechanism which is most likely applicable across all enzymes of the PL7 family as well as other PL families.

Alginates are linear anionic polysaccharides of 1,4-linked β-D-mannuronic acid (M) and its C5-epimer α-L-guluronic acid (G)[1] (Fig. 1a). They are found in brown seaweed cell walls, where they account for 10–45% of the dry weight[2], and can also be produced by bacteria from the genera *Azotobacter* and *Pseudomonas* as an exopolysaccharide[3]. Alginates are synthesized as polyM, and they can be modified by alginate C5-epimerases at the polymer level, resulting in the formation of the different G- and mixed MG blocks. Such modifications greatly affect the physicochemical properties of the alginate polysaccharides, as the G blocks can bind $Ca^{2+}$ (and other divalent ions) resulting in the formation of hydrogels[4]. Due to their physicochemical properties, alginates have attracted industrial interest, notably in food and biomedical applications[5–7]. Approximately 45,000 metric tons of alginates and alginate oligosaccharides are produced industrially per year by extraction from harvested or farmed brown seaweed, with a global market value of about US$900 million[8,9].

The degradation of alginates is catalyzed by alginate lyases (ALs), which are reported in 17 of the 44 polysaccharide lyase (PL) families in the Carbohydrate Active enZyme database (CAZy)[10]. These enzymes can be classified either as *endo*-acting, which cleave the alginate

[1]Departament de Química Inorgànica i Orgànica (secció de Química Orgànica) & IQTCUB, Universitat de Barcelona, Barcelona, Spain. [2]Section for Protein Chemistry and Enzyme Technology, Department of Biotechnology and Biomedicine, Technical University of Denmark, Lyngby, Denmark. [3]Norwegian Biopolymer Laboratory (NOBIPOL), Department of Biotechnology and Food Sciences, NTNU Norwegian University of Science and Technology, Trondheim, Norway. [4]Novo Nordisk Foundation Center for Biosustainability, Technical University of Denmark, Lyngby, Denmark. [5]Department of Molecular and Structural Biochemistry, North Carolina State University, Raleigh, NC, USA. [6]Neutron Scattering Division, Oak Ridge National Laboratory, Oak Ridge, TN, USA. [7]Institució Catalana de Recerca i Estudis Avançats (ICREA), Passeig Lluís Companys, Barcelona, Spain. [8]Present address: SINTEF Industry, Oslo, Norway. [9]Present address: Novo Nordisk A/S, Gentofte, Denmark. [10]Present address: Novo Nordisk Pharmatech A/S, Køge, Denmark. ✉e-mail: c.rovira@ub.edu; cpwk@novonordisk.com

https://doi.org/10.1038/s41467-025-56754-5

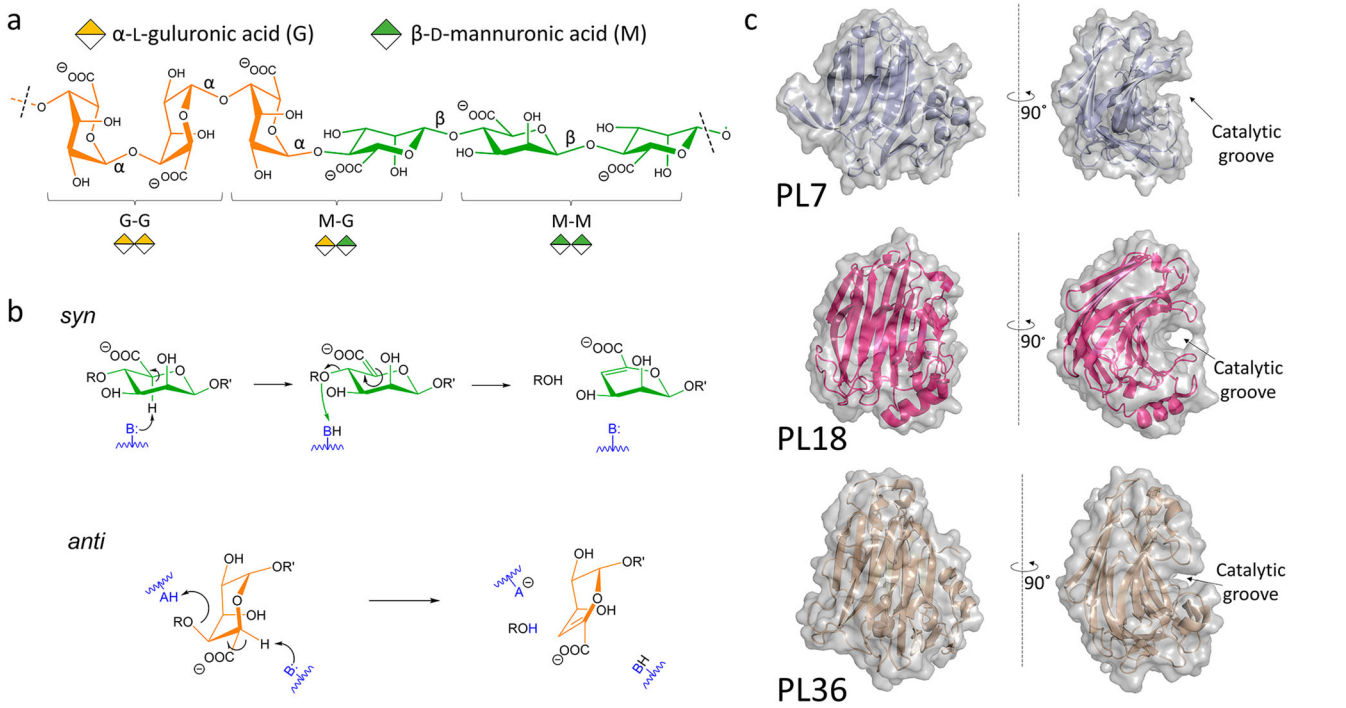


**Fig. 1 | Alginate degradation. a** Stylized chemical structure of alginate. The unit blocks, α-L-guluronic acid and β-D-mannuronic acid, are colored orange and green, respectively. **b** Chemical reactions catalyzed by alginate lyases (ALs). The *syn* reaction is presented above, while *anti* reaction is shown below. Acid and base residues, which belong to the enzyme, are denoted as A and B, respectively, and colored in blue. **c** Structure representation of a PL7 (at the top, PDB 6YWF), a PL18 (in the middle, PDB 4Q8K), and a PL36 (at the bottom, PDB 6KCW) to show the shared jelly roll folding. A rotation of 90° over the *Y* axis highlights the characteristic solvent-exposed catalytic groove where they bind to the polymer.

polysaccharides in the middle of the chain, or *exo*-acting, which cleave the polysaccharide, or more often the AOSs, by attacking one of the terminal ends. Whereas the *endo*-acting ALs initially release alginate oligosaccharides (AOS) that often are further degraded to di- and tri-AOS, the *exo*-acting attack either the reducing end (C1) or the non-reducing (C4) end to liberate a monomer[11–13]. The increased use of alginates in industrial applications has led to an interest in controlling their modification by enzymatic processing. However, our understanding of the mechanisms by which enzymes catalyze alginate modifications is incomplete due to the lack of catalytically competent Michaelis–Menten structures in complex with substrate and products, limiting our ability to tailor-make alginates and AOSs[7,14,15].

PLs cleave O'-C4 glycosidic bonds via a β-elimination reaction, leading to the formation of the 4,5-unsaturated sugar 4-deoxy-L-erythro-hex-4-enopyranosyluronic acid (denoted as Δ) at the non-reducing end of the released product[11,16] (Fig. 1b). A catalytic base (usually a negatively charged tyrosine or a histidine)[15] is expected to abstract the H5 proton from the sugar moiety at subsite *+1*, resulting in the formation of an unsaturated bond between C4 and C5. The bond cleavage is assisted by the transfer of a proton from a general acid to the glycosidic oxygen[16] (Fig. 1b). The reaction can take place in *syn* or *anti*, depending on whether the abstracted proton is on the same side of the departing glycosidic oxygen (*syn*) or it is on the opposite side (*anti*), with respect to the sugar ring (Fig. 1b). In the *syn*-elimination, a single residue, typically a tyrosine[17], acts as both catalytic base and acid[17,18], whereas two residues are needed when the reaction is *anti* [3,15]. The identity of the catalytic base and the general acid remains unknown for several PLs. In addition, fundamental aspects of the catalysis, such as whether the reaction is concerted or stepwise, are unanswered.

The PL7 family holds the largest number of ALs that degrade alginates. This family harbors members that specifically degrade M, G or MG blocks in alginates, and some that are able to degrade two or three different blocks in *endo* or *exo* fashion[12,15,17]. Crystal structures, mainly originating from bacterial enzymes, have revealed that PL7 enzymes display a β-jelly roll fold (Fig. 1c and Supplementary Figs. 1 and 2)[12,17], which is shared with other PL families such as PL18[19] and PL36[20], that forms a groove harboring the active site (Fig. 1c). Some PL7 members, such as the G-specific enzyme from *Sphingomonas* sp. A1, have been suggested to employ an *anti* β-elimination mechanism[21,22]. Other PL7 enzymes, such as the *Flavobacterium* sp. alginate lyase A (FlAlyA), were suggested to follow a *syn* β-elimination mechanism to degrade its preferred substrate polyM, based on crystal structure data and mutational analysis[17]. Such a mechanism was also recently proposed for the β-D-glucuronan lyase TpPL7A from the fungus *Trichoderma parareesei*[23]. However, the reaction mechanism of ALs remains unresolved due to either low resolution of the crystal structures or misplacement of substrates from subsites *−1* and *+1* due to enzyme mutations[21,22,24]. A recent high-resolution[24] crystal structure of a PyAly from the alga *Neopyropia yezoensis* in complex with PentaM (Supplementary Fig. 2c) revealed that two loops around the substrate binding cleft determine the distribution of products. Unfortunately, catalytically relevant substrate–enzyme interactions at the *−1* and *+1* subsites could not be analyzed due to the mutation of critical active site residues (H125A/Y223A). Therefore, detailed characterization of the active site and the catalytic mechanism of PL7 enzymes and ALs remains elusive.

Here, we employ a multidisciplinary approach, including single crystals X-ray and neutron diffraction, NMR spectroscopy, and QM/MM simulations to uncover substrate recognition and the molecular mechanism for M-specific PL7 enzymes. Time-resolved NMR was used to follow the reactions of two PL7 members *Ps*Alg7A and *Ps*Alg7C, from the marine fungus *Paradendryphiella salina*, affirming that they are endolytic and M-specific. In addition, we obtained high-resolution X-ray crystal structures of the two alginate lyases in complex with M oligosaccharides, which, combined with neutron diffraction structures

https://doi.org/10.1038/s41467-025-56754-5

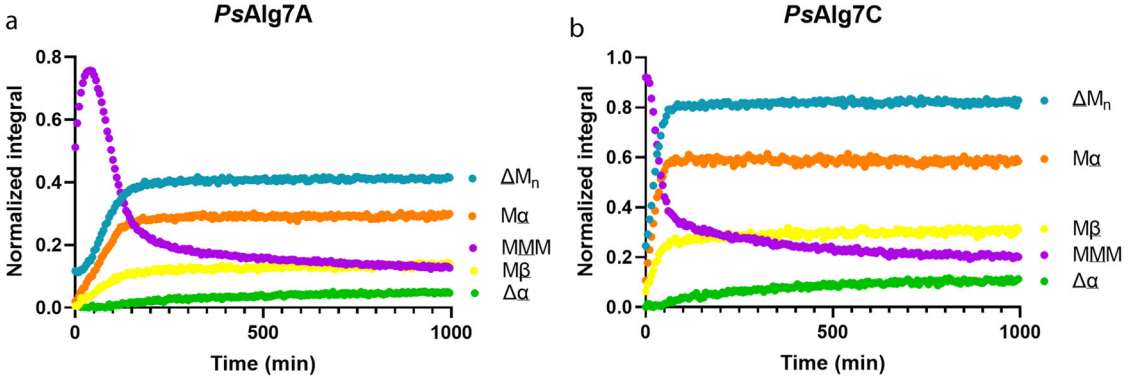


**Fig. 2 | Time-resolved $^{13}$C-NMR spectra results of $^{13}$C1-enriched polyM treated with *Ps*Alg7A or *Ps*Alg7C.** Each reaction was conducted in 3 mm NMR tubes at 25 °C with 8.7 mg/mL enzyme in 170 µL of substrate buffer solution (10 mg/mL $^{13}$C1-polyM substrate in 5 mM Na-acetate, pD 5.5 with 100 mM NaCl and 1.5 mM $ZnCl_2$ in 99.9% $D_2O$) and 10 µL of 147.5 mg/mL *Ps*Alg7A incubated at 25 °C. Pseudo 2D time-resolved spectra were recorded by acquiring 1D carbon spectra every 5 min for a total of 21 h 20 min. **a** shows the reaction for *Ps*Alg7A, and **b** shows the reaction for *Ps*Alg7C. MMM is the internal mannuronate in polyM substrate, and abbreviations of the products formed are: $\underline{\Delta M}_n$ C/H-1 signal of 4-deoxy-L-erythro-4-hexenopyranouronate at the non-reducing end of a mannuronate oligomer/polymer, $M\underline{\alpha}$ C/H-1 signal of α reducing end of mannuronate oligomer/polymer, $M\underline{\beta}$ C/H-1 signal of the β reducing end of mannuronate oligomer/polymer, $\Delta\underline{\alpha}$ signifies the C/H-1 signal of an α reducing end of mannuronate dimer with 4-deoxy-L-erythro-4-hexenopyranouronate at the non-reducing end.

of *Ps*Alg7C, informed QM/MM simulations of *Ps*Alg7A that provided a precise atomistic picture of the reaction coordinate. The simulations confirm the *syn* β-elimination mechanism and reveal that the reaction takes place in one-step, with a tyrosine acting as both catalytic base and acid, and involves the formation of a carbanion-type species at the transition state. Altogether, we provide an atomic description of the mechanism of action of a PL acting on alginate.

## Results

### Time-resolved product formation

The endolytic enzymes *Ps*Alg7A and C are part of the marine fungus *P. salina* metabolization of alginates. Data from previous work suggest that *Ps*Alg7C (pH optimum 8) most likely takes part in the saprophyte's initial attack on the seaweeds cell wall, while *Ps*Alg7A (pH optimum 5), together with an exolytic PL8 alginate lyase, finalize the degradation of the M-blocks in alginates[13,25].

The mode of action and product formation for *Ps*Alg7A was studied with time-resolved NMR on $^{13}$C1 label polyM substrate. *Ps*Alg7A produced oligomers with unsaturated end (Δ) as small as dimers, but no unsaturated monomer was formed (Fig. 2a and Supplementary Figs. 3 and 4). The signal for the unsaturated end (C1Δ at 102.8 ppm) in trimers or oligomers (> DP 2) was present from the beginning of the reaction. In comparison, a slowly increasing signal for the unsaturated end (C1Δ at 102.5 ppm) in dimers appeared later. Based on the integrals (for C1 of unsaturated ends and ratio conformation), the distribution of the reaction products was ~84% trimers or oligomers and ~16% dimers. Looking at the formation of reducing ends, the signals α (96.2 ppm) and β (96.3 ppm) conformers in the unsaturated triMs or oligomers were present from the start of the reaction, while the α reducing end (95.9 ppm) of dimers appeared later. Altogether, the time-resolved NMR results strongly indicate that *Ps*Alg7A displays an endolytic mode of action, producing mainly unsaturated triMs and oligomers of a higher degree of polymerization than three on the polyM substrate. *Ps*Alg7C exhibits a similar endolytic mode of action and product formation (Fig. 2b and Supplementary Figs. 5 and 6).

### The overall structure of PsAlg7A and C and their relation to the structure of other PL7 members

The crystal structures of *Ps*Alg7A and C were determined at 0.82–2.00 Å resolution at pH 4 and 5.5, respectively (a summary of all determined structures is presented in Supplementary Table 1, while data processing statistics are described in Supplementary Table 2) at which *Ps*Alg7A and C retain ~30 and ~20% relative activity[13]. Overall, the electron density maps for the proteins, and the ligands were well-defined (Fig. 3a–d). The tertiary structure of *Ps*Alg7A and C resembles that of other PL7 members, composed of a single β-jelly roll domain with an inner and outer convex anti-parallel β-sheet (Fig. 3a–d and Supplementary Figs. 7 and 9). Analysis of the *Ps*Alg7A structure versus data in the Protein Data Bank (www.pdb.org)[26] using the DALI server[27] revealed that the closest structural homolog for *Ps*Alg7A is indeed *Ps*Alg7C ($C_\alpha$ r.m.s.d. is 0.37 Å, for 166 atom pairs).

The structure of *Ps*Alg7A and C differ from other structurally determined PL7 members, except for PyAly from algae *Neopyropia yezoensis* (PDB ID 7W13)[24], by the presence of two extended β-strings at the non-reducing end of the binding cleft (PsAlg7A: V142–I147 and V150–V155. PsAlg7C: I136–L141 and V144–F149) that form a lid-like structure on top of the substrate (Supplementary Fig. 9). The crystal structures show that the two β-strings form interactions with the soaked PentaM and HexaM substrate in *Ps*Alg7A and C (Fig. 3a–d and Supplementary Figs. 7 and 8), implying that they are probably involved in substrate binding. These two additional β-strings are not present in the β-glucuronan lyase *Tp*PL7A from the terrestrial fungus *T. parareesei* (Supplementary Fig. 9)[23], suggesting that this extension of the active site groove could be limited to alginate lyases from marine eukaryotes or may define substrate selectivity. A structural comparison of PL7 alginate lyases previously suggested to target different linkages in alginate did not reveal any obvious differences in the overall structures with respect to our structures (Supplementary Fig. 9). Interestingly, even though our structures provide a high definition of the enzyme subsites (mainly, because of the low impact of the Tyr-Phe mutation), the location of the sugar units is very similar to some of the previous structures, in particular structures of AlyC3, AlyA1-II and *Py*Aly double mutants in complex with various oligosaccharide substrates (Supplementary Fig. 2).

The substrate binding groove of ALs is, in general positively charged, which favors the binding of the negatively charged substrate[15]. This is also the case for both *Ps*Alg7A and *Ps*Alg7C (Fig. 3e, f and Supplementary Fig. 10). However, the binding groove is less positively charged for *Ps*Alg7A (Fig. 3e) (even at a lower pH), which may explain the seven-fold higher $K_m$ of *Ps*Alg7A (17.4 mM) compared to *Ps*Alg7C (2.4 mM) towards polyM[13]. This difference could also explain the large difference in catalytic turnover rates, with *Ps*Alg7C acting more than three times faster on polyM than *Ps*Alg7A.

https://doi.org/10.1038/s41467-025-56754-5

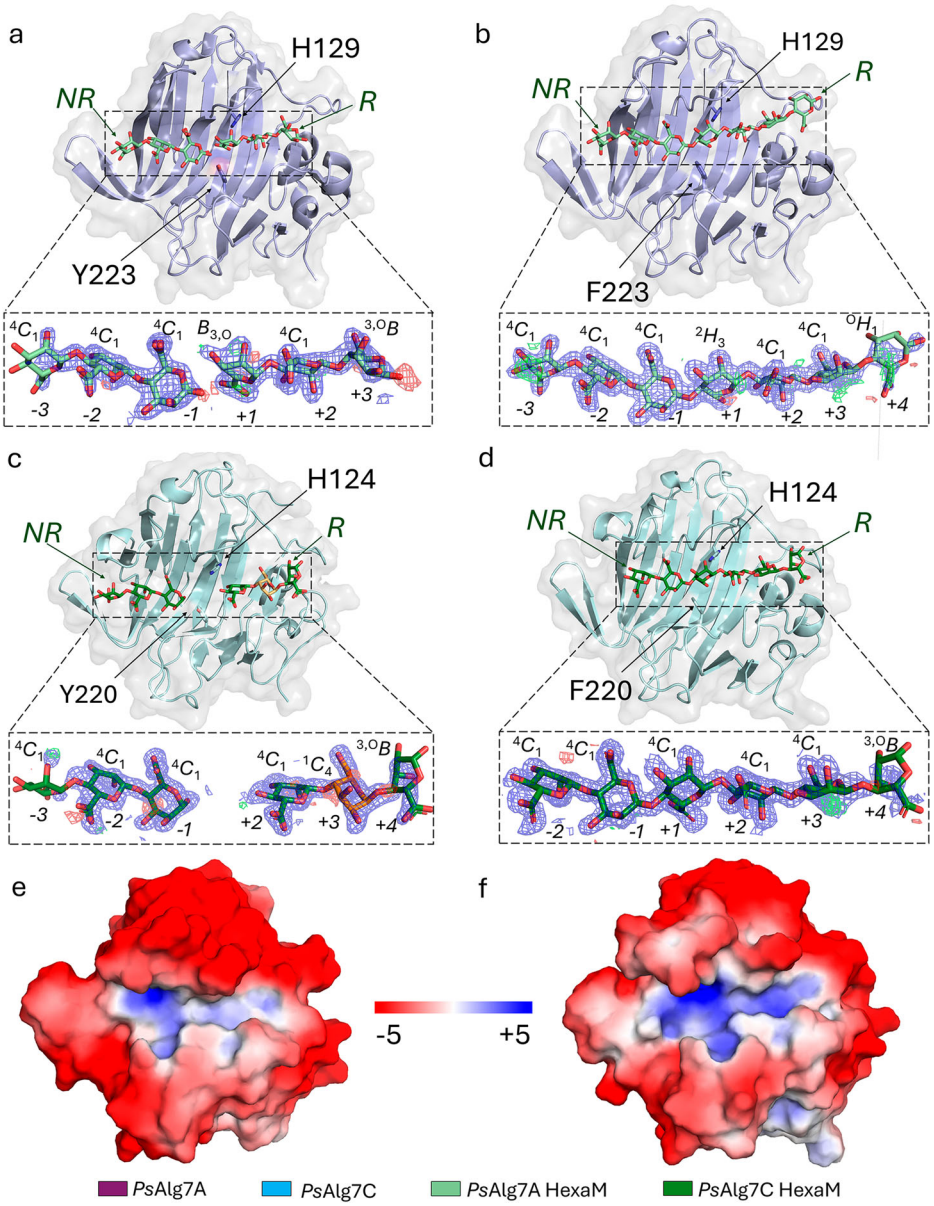


**Fig. 3 | *Ps*Alg7A and C active site architecture. a** *Ps*Alg7A (light purple) soaked with PentaM (light green), **b** *Ps*Alg7A-Y223F (light purple) soaked with HexaM (green), **c** *Ps*Alg7C (cyan) soaked with HexaM (M moieties: dark green; G moieties: orange), and **d** *Ps*Alg7C-Y220F (cyan) soaked with HexaM (M moieties: dark green; G moieties: orange) (NR and R indicate the non-reducing end and reducing end, respectively). The observed AOSs are longer than the AOSs used for soaking likely because they are accommodated in two or more different ways in the active sites. **e** Electrostatic plot of *Ps*Alg7A at pH 5 and **f** electrostatic plot of *Ps*Alg7C at pH 8 with electron density maps, 2Fo-Fc (blue mesh) contoured to 1.0σ with a cutoff at 1.6 Å for C and fc-fo (green and red) contoured to +3.0 and −3.0σ, respectively, with a cutoff at 1.6 Å for C.

### *In crystallo* substrate cleavage reveals the active site

Structures of five PL7 ALs in complex with different alginate oligosaccharides have been reported (Supplementary Fig. 2), revealing a hydrogen bond network and stacking-like interactions important for positioning the substrate in the active site groove[21,22,24]. All these complex structures were obtained for catalytically inactive mutants, in which one or more putative essential residues were mutated. Here, we were able to soak M oligosaccharides with a degree of polymerization (DP) 4–6 into crystals of *Ps*Alg7A (Supplementary Fig. 7), resulting in *in crystallo* cleavage of the sugars (1.46–1.87 Å resolution, Supplementary Tables 1 and 2). This confirmed the *−1* and *+1* subsites for PL7 family members that define the location of the scissile bond (Fig. 3a). Previously, these subsites were only tentatively assumed based on the positions of the presumed catalytic tyrosine and histidine relative to the uronic acids in the complex structures[21,22,24]. The negative subsites (Fig. 3a–d) indicate the position of the non-reducing end of the substrate, while the positive subsites indicate the reducing end[28]. TetraM, PentaM, and HexaM oligosaccharides were found to span subsites *−3* to *+3* (Supplementary Fig. 7), suggesting that TetraM and PentaM are both accommodated in two or more different ways in the active sites of the different *Ps*Alg7A molecules constituting the crystal.

Attempts to perform *in crystallo* substrate cleavage for *Ps*Alg7C were unsuccessful. The structures (Supplementary Fig. 8), determined at 1.09–1.24 Å resolution, showed that M oligosaccharides (DP 2–6) are present at negative and positive subsites, but the *+1* subsite is unoccupied (Fig. 3c and Supplementary Fig. 8). However, this subsite is occupied in both inactive mutants *Ps*Alg7C-H124N and *Ps*Alg7C-Y220F (Figs. 3d, f, 5a and Supplementary Fig. 8) (discussed further below), which crystallized in space groups $C12_1$ and $P12_11$, and $P1$, respectively (Supplementary Table 2), whereas *Ps*Alg7C, crystallized in space group

https://doi.org/10.1038/s41467-025-56754-5

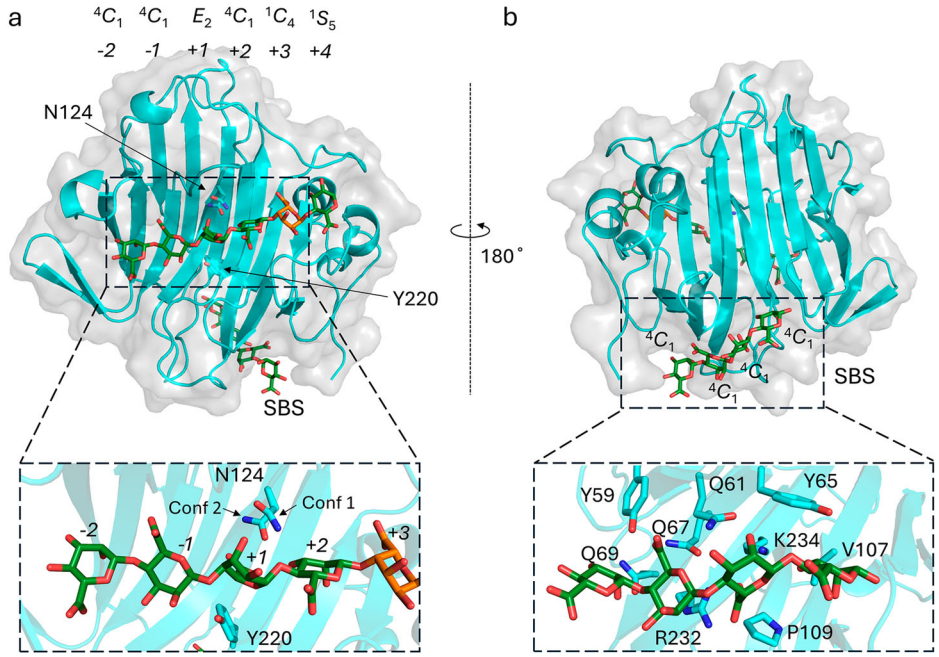


**Fig. 4 | *Ps*Alg7C-H124N (cyan) soaked with PentaM (dark green). a** Active site groove and **b** the surface binding site (SBS). Amino acid residues are shown as sticks, highlighting N124 conformations in (**a**) and residues within 4 Å of the tetrasaccharide in (**b**). The G moiety in (**a**) is colored in orange.

$P2_12_12_1$. A loop from a neighboring molecule in the crystal lattice containing S228 was found to pose steric hindrance on the carboxylic group of the M moiety at subsite *+1* (Supplementary Fig. 11), precluding productive binding. A G moiety was consistently observed at subsite *+3* (Fig. 3c and Supplementary Fig. 8), which may stem from impurities in the M oligosaccharides, suggesting that *Ps*Alg7C has a preference for G moieties at this subsite or that a C5 epimerization reaction took place. A G moiety was also observed at subsite *+3* in *Ps*Alg7C-H124N soaked with PentaM (Fig. 4a).

## Michaelis–Menten-like complexes

To obtain Michaelis–Menten-like complexes of *Ps*Alg7A and *Ps*Alg7C, the inactive mutants *Ps*Alg7A-Y223F, *Ps*Alg7C-H124N and *Ps*Alg7C-Y220F soaked with M oligosaccharides (TetraM, PentaM and HexaM) were crystallized (Fig. 3b–d and Supplementary Figs. 7, 8, and 10). The corresponding structures were determined at 1.45–1.81 Å (*Ps*Alg7A-Y223F), 1.05–1.51 Å (*Ps*Alg7C-Y220F) and 0.87–1.13 Å resolution (*Ps*Alg7C-H124N). The structures show that the TetraM and PentaM substrates span subsites *−2* to *+3* in *Ps*Alg7A-Y223F (Supplementary Figs. 7 and 8), while HexaM spans *−3* to *+4* (Fig. 3b and Supplementary Fig. 10B). As found for the product complexes, this suggests that the M oligosaccharides can be accommodated in two or more different ways in the active site. Except for G moieties observed at subsite *+3*, the M moieties in the *Ps*Alg7C complex structures resemble those observed in *Ps*Alg7C-Y220F (Fig. 3c, d).

The structure of *Ps*Alg7A-Y223F soaked with HexaM reveals a highly complex hydrogen bond network, which is probably responsible for the substrate accommodation in the active site groove (Supplementary Fig. 12), optimizing enzyme interactions with the M moieties. The majority of the enzyme–substrate interactions are mediated by water molecules, while some direct hydrogen bonds are observed (Supplementary Fig. 12). A similar hydrogen bonding network was observed in the structures of *Ps*Alg7A-Y223F soaked with TetraM and PentaM, respectively, confirming its importance for substrate recognition. Similarly, a highly complex hydrogen bond network was observed in the structure of *Ps*Alg7C-Y220F (Supplementary Fig. 13).

In a recent study, Zhang et al.[24] showed that two arginine residues and a glutamine (R82/R86/Q127 in *Ps*Alg7A; R76/R80/Q122 in *Ps*Alg7C) are conserved in all PL7 members irrespectively of specificity. These interact with the C5 carboxylic groups at subsites *+1* and *+3* (Supplementary Fig. 10) resulting in similar spatial orientation of the C5 carboxylic groups irrespective of the specificity[24]. Additional hydrogen bonds, including water-mediated ones, were formed to the C5 carboxylic group at subsite *+3* (Supplementary Figs. 12 and 13). Interestingly, we did not observe any hydrogen bonds to the C5 carboxylic group at *+2* (Supplementary Figs. 12 and 13), which likely allows the sugar to have some conformational freedom, enabling the binding of all alginate block types at the positive subsites. At subsite *+2*, putative hydrogen bonds were observed to O2 (Q42 and S46 *Ps*Alg7A; Q36 *Ps*Alg7C) and O3 (K219 *Ps*Alg7A; K216 *Ps*Alg7C) (Supplementary Figs. 12 and 13). The residues interacting with the sugar moieties at the negative subsites are not conserved within the PL7 family, hence this likely determines their specificity[24]. At subsite *−1*, an arginine (R161 Ps*Alg*7A; R155 Ps*Alg*7C) interacting with the C5 carboxylic group is found in both Ps*Alg*7A and C (Supplementary Figs. 12 and 13), which highlights the importance of the orientation of the moiety at this subsite. The hydrogen bonds to the C5 carboxylic group at the remaining negative subsites are not conserved (Supplementary Figs. 12 and 13), which could explain why *Ps*Alg7C is able to accommodate a G moiety at subsite *+3*.

## Active site structure conservation

The overall structures of *Ps*Alg7A-Y223F-HexaM and *Ps*Alg7C-Y220F-HexaM complexes resemble each other (Fig. 3b–d and Supplementary Fig. 10B). Their most noteworthy difference is in R161 (*Ps*Alg7A) and R155 (*Ps*Alg7C) at subsites *−1* and *+1*, which are observed in different conformations (Supplementary Fig. 10B). Another difference is that A169 (*Ps*Alg7A) at subsites *−2* and *−3* is replaced by the bulky F165 in *Ps*Alg7C (Fig. 5a–f and Supplementary Figs. 10A and 10B). However, this does not affect the overall structure of the active site (Figs. 3a–d, 6, and Supplementary Fig. 10).

The importance of the hydrogen bonding network mentioned above (Supplementary Figs. 12 and 13) is underlined by the structural conservation of several water molecules mediating the hydrogen bonds between the M moieties at subsites *−1* and *+1*. These water molecules are observed in similar positions in both *Ps*Alg7A and C

https://doi.org/10.1038/s41467-025-56754-5

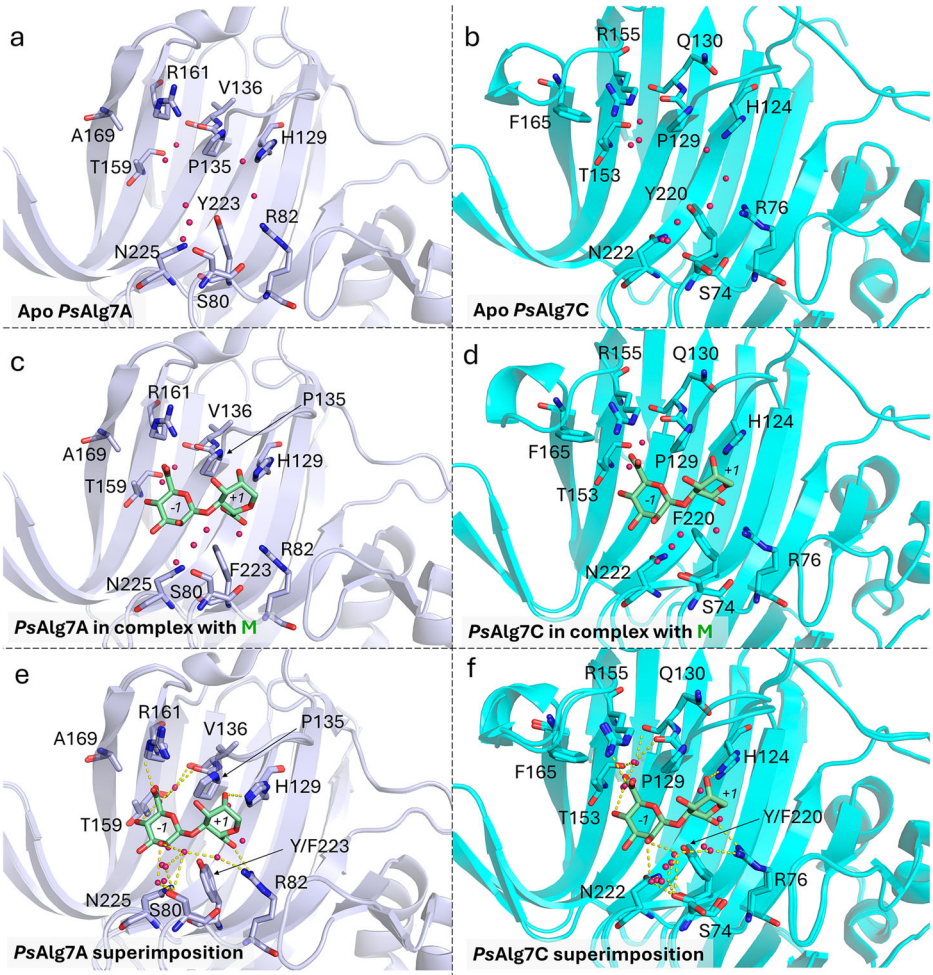


**Fig. 5 | Organization of binding sites in the presence and absence of the ligand.** **a** The *apo* structures of *Ps*Alg7A and **b** *Ps*Alg7C exhibit conserved water molecules and residue orientations, **c** which are compared with the *Ps*Alg7A-Y223F and **d** *Ps*Alg7C-Y220F mutants soaked with HexaM. For simplicity, only sugars at subsites *−1* and *+1* are shown. Conserved water molecules, residues, and putative hydrogen bonds formed with the M moieties at subsites *−1* and *+1* are highlighted in the superimposed *apo* and complex structures for **e** *Ps*Alg7A and **f** *Ps*Alg7C. Yellow dotted lines indicate putative hydrogen bonds.

*apo* and complex structures (Fig. 5a–f). Overall, the active site changes only little upon ligand binding and from one enzyme to another.

## Mutations affect the β-D-mannuronic acid moieties' conformation

Most of the M moieties of the PsAlg7A-Y223F-HexaM complex are present in the $^4C_1$ conformation in the *Ps*Alg7C-Y220F-HexaM complex, except the one at subsite *+1*, which adopts a distorted $^2H_3$ conformation (Fig. 3b). This is also the case with the Penta- and TetraM complexes (Supplementary Fig. 8). This unusual conformation[29] is probably due to the Y223F mutation, which causes R82 to interact strongly with the oxygen of the sugar at the *+1* subsite rather than interacting with the oxygen atom of the negatively charged Tyr (Fig. 3b and Supplementary Fig. 10). Further, the structure of *Ps*Alg7C-H124N shows that the mutation apparently results in a distortion of the M moieties, most evident for the one in the *+1* subsite (Fig. 4a and Supplementary Fig. 8). This distortion is likely a result of the loss of the interaction between H124 and the 2-OH group of the sugar unit at the *+1* subsite (Fig. 4a), leading to a displacement of the scissile bond. In fact, N124 is observed in two different conformations when in complex with M oligosaccharides (Fig. 4a), suggesting that the asparagine residue does not interact with the M moieties. This is likely the reason for the almost complete loss of activity upon mutating the wild-type histidine that was previously observed in other PL7 members[22,23].

## Surface binding site

A surface (or secondary) binding site (SBS) was observed in the crystal structure of *Ps*Alg7C-H124N in soaked with PentaM on the opposite of the active site groove (Fig. 4b). SBSs hold a diversity of functions and share many roles with the more known carbohydrate-binding domains (CBMs), which are domains separate from the catalytic domains. In contrast to CBMs, SBSs are located at a certain distance of the active site on the catalytic domains. Although some SBSs have previously been shown to be important for the activity and functionality of their parent catalytic domain[30–32], no SBSs have been previously identified in PLs. Four M moieties are observed at the SBS on *Ps*Alg7C-H124N, which all interact with *Ps*Alg7C through hydrogen bonds (Fig. 4b) that potentially can discriminate for M moieties. The fact that AOS accommodate at the SBS in only one of the *Ps*Alg7C structures does suggest that the site is not essential for *Ps*Alg7C's activity, but likely a crystallization artifact. However, its role, if any, in *Ps*Alg7C's degradation of M-blocks in alginate requires further investigations, which is beyond the scope of this study.

## Protonation states of putative catalytic residues

To investigate the protonation states of the residues interacting with the substrate, neutron diffraction structures of *Ps*Alg7C before and after soaking with PentaM were obtained. These structures were determined at 2.15 Å resolution (see Supplementary Table 3 for statistics). Of particular interest, the neutron structures suggest that the

hydrogen(deuterium) of Y220 is disordered prior to substrate binding but become ordered, and likely engages in hydrogen bonding, in the product complexes (Fig. 6). Conversely, H124 holds only one proton (i.e., it is a neutral residue) in both the substrate-free structure and the product complex (Fig. 6a, b). This strongly suggests that Y220 is the catalytic base that abstracts a proton from the saccharide at the *+1* subsite during catalysis. Remarkably, in silico replacement of F223 to Tyr in *Ps*Alg7A-Y223F-HexaM shows a clear short distance between the Tyr oxygen atom and the H5 atom of the saccharide at the *+1* subsite (Supplementary Fig. 14), supporting a role of the Tyr as general base in catalysis. Given that the expected p$K_a$ for tyrosine in solution is ~10[33], we hypothesize that the microenvironment surrounding this residue is influencing its ionization, thereby lowering its p$K_a$. This is supported by various enzymatic studies documented in the literature where tyrosine is deprotonated due to the presence of nearby residues. Examples include short-chain dehydrogenase/reductase (SDR) enzymes[34], C4 epimerases[35], and UDP-apiose/UDP-xylose synthase[36], where neighbouring positively charged residues contribute to the decreased p$K_a$. Another example is alanine racemase, in which the connection to a histidine, which is itself linked to arginine, is known to reduce the p$K_a$ of the catalytic tyrosine[37]. Upon examining the surrounding residues of Y220, we identified a nearby arginine (R76 in Fig. 6a–c), which we suspect is responsible for the lowered p$K_a$. Notably, this arginine (R82 in *Ps*AlgA) is conserved within the PL7 family and its mutations result in the loss of lyase activity. Even though this has been explained in terms of substrate binding[21], we suggest that these mutations could also potentially affect the ionization state of the catalytic base residue.

While in the neutral form, H124 cannot act as a proton donor, thus it cannot be the catalytic acid. This is consistent with the *syn*-elimination mechanism (Fig. 1b), in which tyrosine is expected to be the only catalytic residue. The present high-resolution X-ray crystal structures indicate that the active site histidine (*Ps*Alg7C: H124 and *Ps*Alg7A: H129) forms a hydrogen bond with the 2-OH of the M saccharide at subsite *+1* (Supplementary Figs. 10 and 12), suggesting that it is in the $N_\delta$ tautomeric form. Together with the results obtained for *Ps*Alg7C-H124N, our results suggest that H124 is essential for the productive binding of the substrate but does not participate in the catalytic reaction.

## Product complexes

The structures of *Ps*Alg7A and C and their mutants in complex with DiM and TriM oligosaccharides provide insight on relevant enzyme–substrate interactions after glycosidic bond cleavage. The structures show that the substrate spans subsites *−3*, *−2*, and *−1*, except for *Ps*Alg7C-Y220F in complex with TriM (Supplementary Fig. 7). This may explain why a build-up of DiM and TriM is observed by time-resolved NMR spectroscopy (Fig. 2 and Supplementary Figs. 3–6). We, therefore, speculate that these structures mimic the enzyme state after leaving group departure, prior to a processive movement of the substrate in the active site groove. Similar to what was observed for *Ps*Alg7A in complex with the TetraM, PentaM, and HexaM products (Fig. 3a and Supplementary Fig. 7), the M moieties of DiM and TriM at subsite *−1* are often found in both α and β configurations (Supplementary Figs. 10A and 7). Y223 (*Ps*Alg7A) and Y220 (*Ps*Alg7C) are both within hydrogen bonding distance from the O1 atom of the M sugar at subsite *−1*. The observed α and β configurations may reflect that tyrosine residues Tyr223 and Tyr220 are not protonated in all molecules within the crystals, as found in the neutron structure of *Ps*Alg7C (Fig. 6).

## Conformation of the substrate β-mannurosyl unit at the *+1* subsite

The structure of *Ps*Alg7A-Y223F soaked with HexaM (PDB ID 7NCZ) was used as the initial template for the molecular dynamics (MD) simulations. In the simulations, the F223 residue was substituted for a tyrosine residue to reconstruct the native enzyme (Supplementary Movie 1). The solution structure Michaelis–Menten complex (MC) was built using Amber 2020 tools (see details in "Methods"). The complex was subsequently minimized and equilibrated for 750 ns (Supplementary Fig. 15). The simulations show that the enzyme–substrate complex remains stable in a catalytically productive configuration, with H129 and Y223 sandwiching the *+1* saccharide, which adopts a $^4C_1$ conformation. The negatively charged oxygen of the putative catalytic base, Y223, is close to R82, forming a salt-bridge interaction. The O atom of Y223 is also very close to the H atom at C5, ready for proton abstraction.

To further confirm the conformation of the *+1* saccharide, we computed its conformational free energy landscape (FEL) using QM/MM metadynamics[38]. This approach has been previously used with success to elucidate substrate conformations in other CAZymes[39]. The use of a QM description of the substrate is necessary to exclude any bias due to the classical force field, which often favors chair conformations[39,40]. The conformational FEL of the *+1* subsite M moiety in *Ps*Alg7A (Supplementary Fig. 16) confirmed that $^4C_1$ is the most stable conformation (the global minimum of the FEL). Remarkably, there is a particularly low-energy region that extends towards $^2S_O$, which is precisely the conformation of the transition state (TS) of the reaction, as described below. Therefore, as previously observed for glycosidases[39], the active site of *Ps*Alg7A is optimized to precisely stabilize the substrate in conformations that are relevant for catalysis.

## Reaction mechanism

One representative snapshot from the classical MD simulations was selected (Supplementary Fig. 15) as the starting point to initiate QM/MM MD simulations of the reaction mechanism. A large QM region (112 atoms) was taken to include part of the substrate and the sidechains of the main residues interacting with the *+1* saccharide (Y223, R82, K219, and Q127) (Supplementary Fig. 17). The simulations were performed with the CP2K program[41,42], using Density Functional Theory (DFT) at the QM region and the Amber-based force fields at the MM region (see more details in the Methods section). The system was equilibrated for 7 ps at QM/MM MD level before starting the simulation of the reaction mechanism.

The chemical reaction (Supplementary Movie 2) was modeled using the OPES enhanced sampling method[43,44], which provides a very efficient exploration of complex energy landscapes, as shown in recent applications to chemical reactions[45]. Two collective variables (CVs) were used to drive the system from reactants to products (see Fig. 7a for CVs definition). The first CV was taken as the distance (d) of the scissile glycosidic bond [CV1 = d(O4-C4), where O4 refers to the O′ atom]. The second CV was taken as a combination of the distances involved in the possible motion of the catalytic proton (H5) [CV2 = d(C5-H5) − d(H5-$O_{Tyr223}$) − d(O4-H5)]. Therefore, CV1 accounts for the cleavage of the glycosidic bond, while CV2 accounts for proton transfer events. Using these CVs, the QM/MM OPES simulation successfully drove the reactants towards the products of the reaction, i.e., TriM and unsaturated $(ManA)_4$. The computed reaction-free energy landscape (FEL) (Fig. 7b) shows two well-defined reactants and products minima, with the latter being lower in energy, separated by a distinct transition state (TS). Therefore, the reaction is concerted and exothermic. The computed reaction-free energy barrier for *Ps*Alg7A (16.5 kcal·mol$^{-1}$) is in very good agreement with the experimental value estimated from the reaction rate[13] (17.3 kcal·mol$^{-1}$), which reinforces the mechanism obtained.

Analysis of the molecular changes along the minimum energy pathway (Fig. 7c, d) shows that the reaction begins by a slight repositioning of R82 (state 1 in Fig. 8), which detaches from Y223 and approaches the endocyclic O5 atom of the *+1* saccharide. This motion, although small, induces a distortion of the *+1* saccharide from the relaxed $^4C_1$ chair to a skew-boat $^2S_O$ conformation, enabling close

https://doi.org/10.1038/s41467-025-56754-5

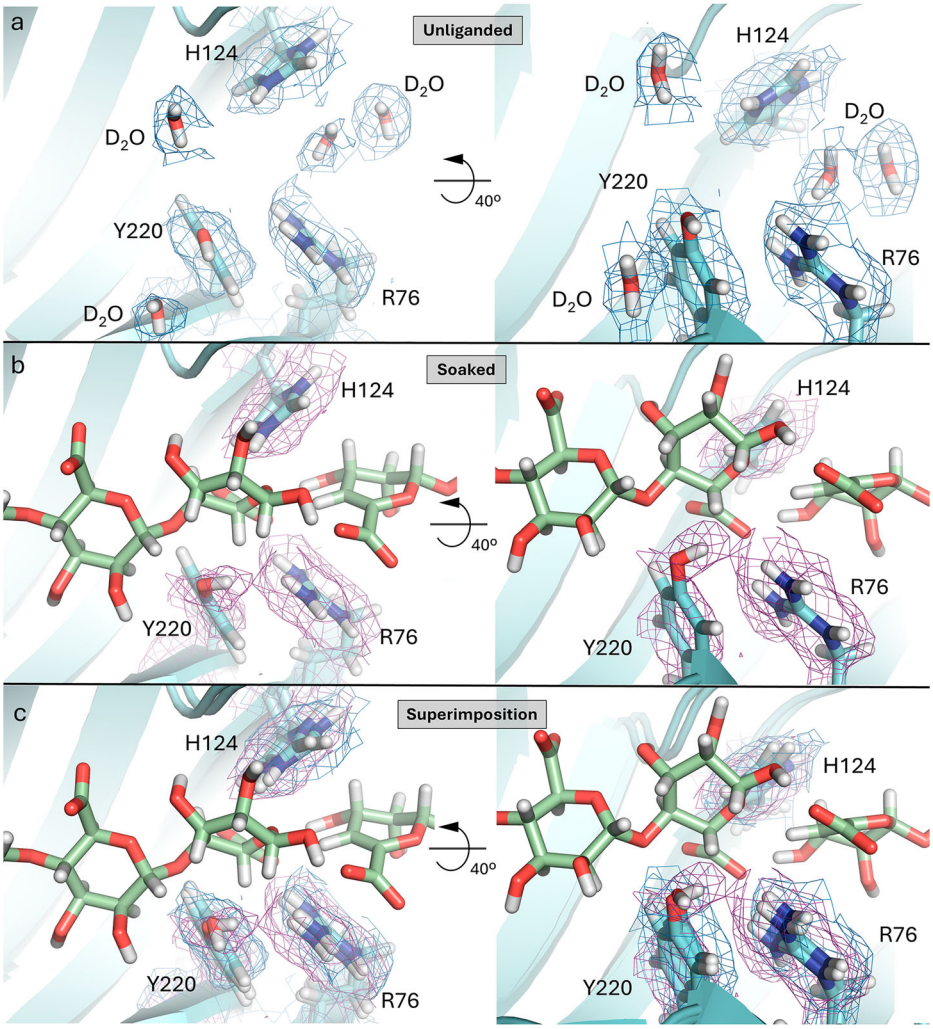


**Fig. 6 | Protonation states of putative catalytic residues.** Structure of **a** *Ps*Alg7C, **b** *Ps*Alg7C soaked with PentaM and **c** superimposition of both. Nuclear density map 2Fo-Fc (blue mesh and magenta mesh for apo and soaked, respectively) contoured at 0.5σ with a cutoff at 1.6 Å. The disordered deuterium was tentatively placed in a riding position on the hydroxyl group of Y220.

contact between the oxygen atom of Y223 and the H5 atom of the *+1* saccharide, which becomes ready for proton transfer. Subsequently, Y223 abstracts the H5 proton (state 2 in Fig. 8) and the C5 atom acquires negative charge (Fig. 7e and Supplementary Table 5). The negative charge on C5 is delocalized over C6, causing both the C4–C5 and C5–C6 bonds to shorten upon reaching the reaction TS (Fig. 7d), which has carbanion character. The cleavage of the glycosidic O4–C4 bond takes place after the TS (state 3 in Fig. 8), just before reaching the products state in which the glycosidic bond is fully broken. The *+1* sugar adopts an envelope ($^2E$) conformation at the reaction products, due to the formation of a double bond between atoms C4 and C5 upon formation of a 4,5-unsaturated sugar (4-deoxy-L-erythro-hex-4-enopyranosyluronic acid). Therefore, even though the reaction-free energy landscape (Fig. 7b) shows a single TS, indicative of a concerted reaction, the reaction is highly asynchronous, with glycosidic bond cleavage taking place after proton transfer. Our simulations also predict a $^4C_1 \rightarrow [^2S_O]^{\ddagger} \rightarrow {}^2E$ conformational itinerary (Fig. 7d) for the β-elimination reaction catalyzed by *Ps*Alg7A.

Further analysis of the species present at the product state (P) reveals that it is a mixture of states in which Y223 can be either neutral or deprotonated. In other words, the H5 proton can be either located at the oxygen atom of Y223 (with the new reducing end being an alkoxide) or at the oxygen atom of the new reducing end (with Y223 being negatively charged). A separate QM/MM MD simulation of the reaction products confirmed that the proton often jumps between both oxygen atoms and the free energy barrier for proton exchange is very small (<1 kcal/mol) (Supplementary Fig. 18), consistent with the analysis of the FEL. Therefore, the reaction products feature a low-energy barrier hydrogen bond between Y223 and the new reducing end. Most importantly, this agrees with the reported neutron diffraction structure of the reaction products, which shows a mixture of Y220 states, protonated and neutral, in *Ps*Alg7C (Fig. 6b).

## Discussion

The reaction mechanism of PLs has been described as a β-elimination reaction, leading to the cleavage of the O'-C4 glycosidic bond and the formation of a 4,5-unsaturated sugar at the non-reducing end of the released product[11,16] (Fig. 1b). However, until now no high-resolution structure with well-defined substrate positions has been reported, hampering an atomistic description of the molecular mechanism. Here we reported high-resolution structures of enzyme–substrate complexes of two PL7 ALs that degrade alginates, i.e. *Ps*Alg7A and *Ps*Alg7C from the marine fungus *P. salina*. We showed by time-resolved NMR that the enzymes are endolytic, M-specific and produce mainly trimers or oligomers with unsaturated ends. The structures include a high-resolution Michaelis–Menten-like complex of a PL7 captured using a single mutant (Y to F), minimally perturbing the active site architecture and, most importantly, with the substrate in a catalytically competent

https://doi.org/10.1038/s41467-025-56754-5

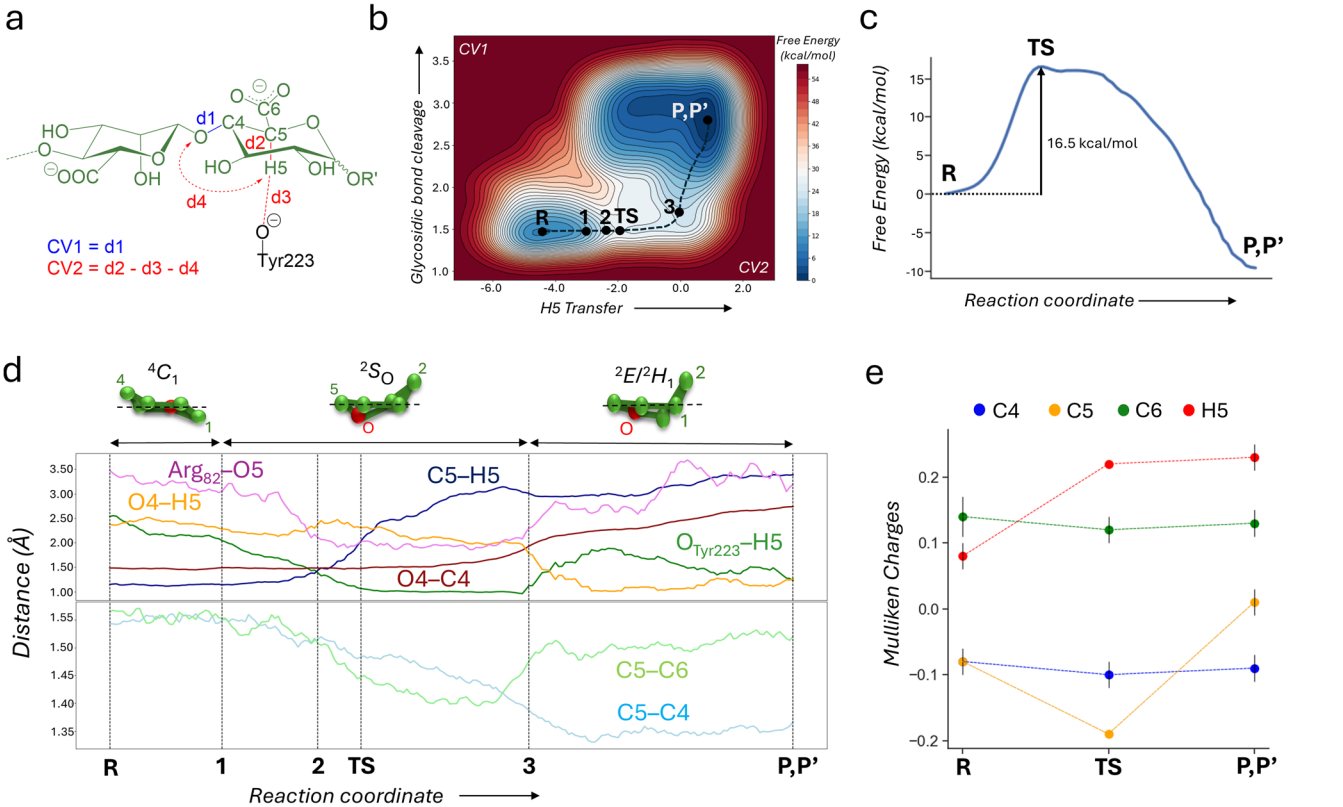


**Fig. 7 | Computational modeling of the *syn* β-elimination reaction catalyzed by *Ps*Alg7A. a** Collective variables used in the QM/MM OPES simulations of the catalytic mechanism of *Ps*Alg7A. **b** Free energy landscape (FEL) obtained from the simulations and minimum free energy pathway defining the reaction coordinate. **c** Potential Mean Force (PMF) along the minimum energy pathway. **d** Evolution of the most relevant distances along the reaction coordinate. **e** Evolution of the Mulliken charges of the main atoms involved in the catalysis of sugar at subsite +1 during the reaction. Data are presented as mean values ± SD, obtained from unbiased QM/MM MD simulations, as described in the methods section (nR = 2000, nTS = 50 and nP = 2000).

position. Together with a neutron diffraction structure, we uncovered the protonation states of the putative catalytic residues Y223/Y220 and H129/H124 (*Ps*Alg7A/*Ps*Alg7C numbering). We showed that both residues are unprotonated, suggesting that only Y223/Y220 is catalytically relevant. In addition, a SBS was found on *Ps*Alg7C (Fig. 4).

The crystal structure of the Michaelis–Menten-like complex of *Ps*Alg7A soaked with HexaM was used for QM/MM simulations of the reaction mechanism, which confirmed the β-elimination reaction and solved the complete mechanism at atomic detail. The reaction takes place in one-step (i.e., a concerted process), but it is highly asynchronous, with proton abstraction by Y223 taking place before the transition state is fully achieved. This is supported by the fact that Y220 is deprotonated in the *apo* neutron structure of *Ps*Alg7C (Fig. 6) but both α and β-conformations of the products are observed after catalysis (Fig. 7 and Supplementary Fig. 10A).

Our findings of a concerted yet asynchronous mechanism reconciles previous experimental studies which were interpreted in terms of either concerted or stepwise reactions. Our simulations also reveal the carbanion nature of the TS and the occurrence of a low-energy barrier hydrogen bond between Y223 and the new reducing end at the reaction products.

The *+1* sugar adopts a relaxed chair conformation ($^4C_1$) at the Michaelis–Menten complex, but evolves gradually towards $^2S_O$ at the TS, thanks to a subtle but important motion of Y223 and R82, delineating a $^4C_1 \rightarrow [^2S_O]^{\ddagger} \rightarrow {}^2E$ conformational itinerary. Importantly, the conformations attained by the *+1* sugar during the reaction lie in a low-energy region of the conformational FEL of the substrate at the Michaelis–Menten complex. This indicates that, similar to what has been observed in glycosidases[1,2], the active site of PsAlg7A is preorganized for catalysis not only in terms of having the catalytic residues at the right position, but also by displaying a binding cavity in which only catalytic conformations fit optimally.

The finding of a concerted (one-step) reaction for *Ps*Alg7A clarifies previous kinetic analyses for several PL7 enzymes, where the presence of a reaction intermediate remained ambiguous[16,46]. In the case of the PL8 Chondroitin AC lyase from *Flavobacterium heparinum*, which also undergoes *syn*-β-elimination[47], previous KIE and LFER experiments suggested a stepwise reaction without glycosidic bond breaking in the rate-determining step. However, a semiempirical QM/MM study on a family PL8 hyaluronate lyase[48] found a concerted *syn*-β-elimination reaction. We argue that the kinetic data can also be interpreted in terms of a concerted reaction in which proton abstraction, and not glycosidic bond cleavage, occurs first, as we have found for PL7 (the reaction is highly asynchronous). Structural and kinetic experiments on other PL families such as PL1 and PL10, which undergo anti-elimination, support catalysis through either a stepwise E1cb reaction or a concerted asynchronous E2 reaction[49], consistent with our observations. In both cases, a carbanion species was predicted to be formed, consistent with our results for *Ps*Alg7. Integrating our findings with existing literature, we propose that the concerted but asynchronous reaction that we have found for PL7 (Fig. 8b) may extend to other PL families.

These structural and mechanistic insights mark a significant advance in our understanding of alginate lyase mechanisms, providing avenues for the engineering of ALs for the production of tailor-made alginate oligosaccharides. Additionally, they open up opportunities for designing activity-based probes to identify alginate lyases in fungal and bacterial secretomes.

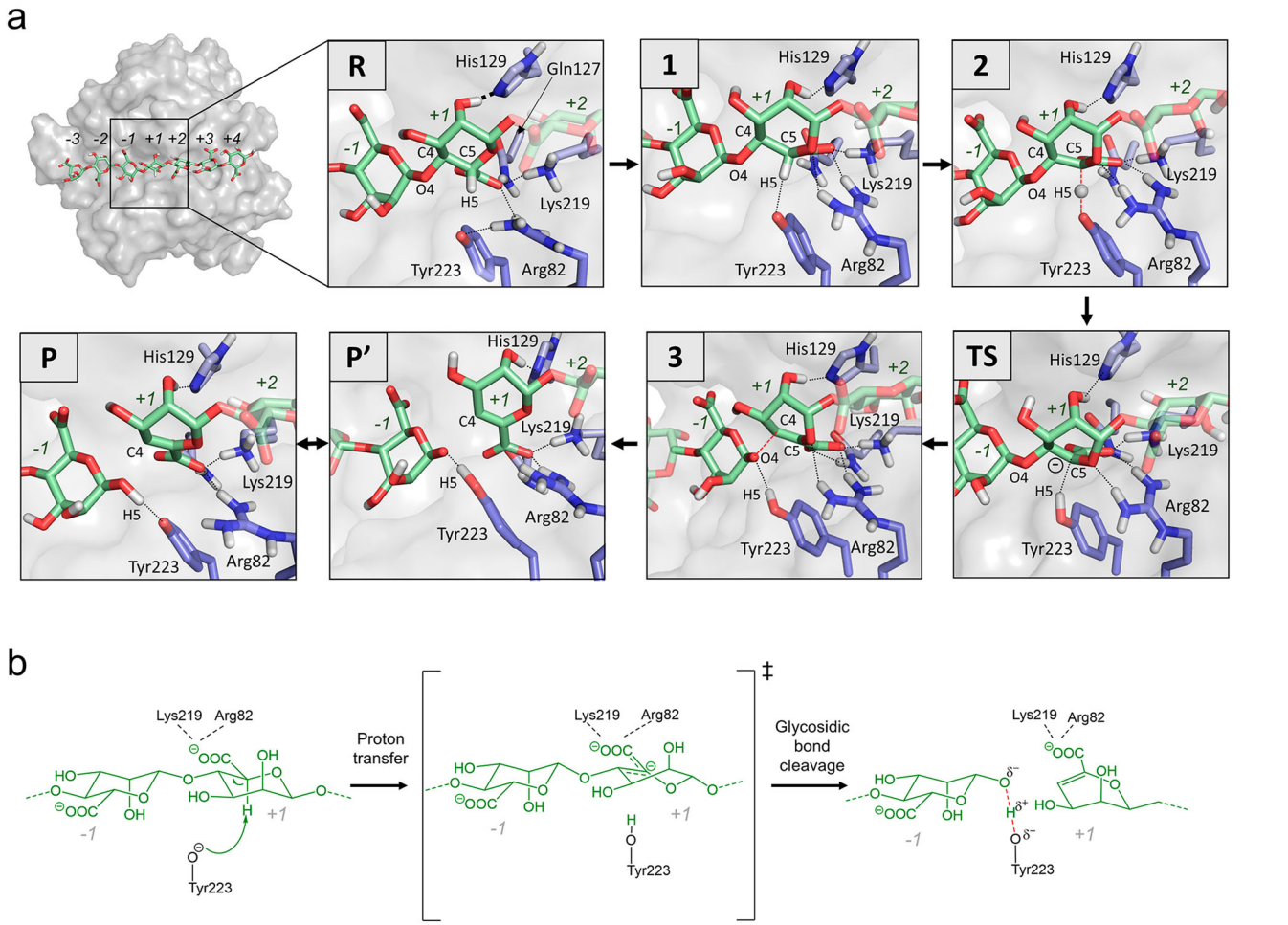


**Fig. 8 | Molecular changes along the reaction coordinate in *Ps*Alg7A.** **a** Representative structures along the reaction coordinate, obtained from QM/MM OPES simulations. Hydrogen atoms that are attached to C atoms have been omitted for clarity, except the H5 atom. **b** Proposed reaction mechanism for *Ps*Alg7A according to all results of this work.

## Methods

### Protein production and site-directed mutagenesis

*Ps*Alg7A-Y223F, *Ps*Alg7C-H124N and *Ps*Alg7C-Y220F were constructed by site-directed mutagenesis using CloneAmp polymerase (Takara), a set of mutagenic primers (see Supplementary Table 4), and pPICzαA/PsAlg7A or pPICzαA/PsAlg7C as template. Plasmid templates were then digested with DpnI at 37 °C overnight, and the resulting PCR products were purified using the illustra GFX PCR DNA and Gel Band Purification Kit (GE Healthcare Life Sciences). The purified PCR products were subsequently transformed into *Escherichia coli* DH5α and plated on LB low salt agar supplemented with Zeocin (25 μg $ml^{-1}$). Positive transformants were selected, and the corresponding plasmids were extracted using the GeneJET Plasmid Miniprep Kit (ThermoFisher Scientific). The validity of all constructs was confirmed through sequencing (Macrogen). Cloning into *Pichia pastoris* X-33 was carried out following the established protocol as in Pilgaard et al.[25].

Expression and purification of *Ps*Alg7A (GenBank acc. nr. VFY81779.1), *Ps*Alg7A-Y223F, *Ps*Alg7C (GenBank acc. nr. CAD6594633), *Ps*Alg7C-H124N and *Ps*Alg7C-Y220F were carried out as in Pilgaard et al.[25]. except that a size exclusion chromatography step on a HiLoad 16/60 Superdex G75 (GE Healthcare) equilibrated with 10 mM Tris-HCl, 150 mM NaCl pH 7 followed the previous purification steps with a flow of 0.5 ml $min^{-1}$. The purity of the obtained fractions was evaluated on 12% SDS-PAGE gels and the pure fractions were pooled and stored at 4 °C (Supplementary Fig. 21).

### Production of $^{13}$C1 labeled polymannuronan

*Pseudomonas fluorescens* Pf20118, a mucoid strain derived from *P. fluorescens* NCIMB 10525 with mutations in mucA and algG[50], was used for mannuronan production. Pf20118 was cultivated in 3 L Applikon fermenters with a medium containing fructose (d-fructose ($^{13}$C1, 99%) from Cambridge Isotope Laboratories, USA) (60 g/L), yeast extract (12 g/L), $(NH_4)_2SO_4{\cdot}H_2O$ (0.6 g/L), $Na_2HPO_4{\cdot}2H_2O$ (2 g/L), NaCl (11.7 g/L), and $MgSO_4{\cdot}7H2O$ (0.3 g/L), at pH 6.8 and 25 °C. Airflow was set to 0.45 VVM initially and adjusted to 0.85 VVM after 10 h. Dissolved oxygen was kept at 20% saturation by adjusting the stirrer speed. To prevent mannuronan degradation, proteases (Neutrase and Alcalase both from Novonesis, Bagsværd, Denmark) were added at 0.1 g/L. Fermentation ended upon carbon source depletion, followed by formalin addition (1%) for conservation, and cultures were stored at 4 °C. Cultures were diluted with 0.2 M NaCl and centrifuged (10,000×*g*, 60 min) to remove bacterial cells. The supernatant alginate was deacetylated by mild alkaline treatment, precipitated with HCl (3 M) to pH <2, and collected by centrifugation (8000×*g*, 15 min)[51]. The precipitate was washed with 0.05 M HCl, dissolved in water adjusted to pH 6.9–7.2 with NaOH (3 M), and precipitated again with NaCl (2 g/L) and 60% isopropanol, followed by centrifugation (6000×*g*, 10 min) and air drying.

### Time-resolved NMR

Each reaction was comprised of 170 μL of 10 mg/mL $^{13}$C1-enriched polymannuronate substrate[50] in buffer (with 99.9% $D_2O$) and 10 μL of

enzyme stock. For *Ps*PL7A (enzyme stock 147.5 μg/mL) the buffer composition was 5 mM NaOAc pD 5.0, 10 mM NaCl, 1.5 mM $ZnCl_2$ and for *Ps*PL7C (enzyme stock 150 μg/mL) the buffer composition was 5 mM HEPES pD 8.0, 100 mM NaCl. All experiments were recorded on Bruker 800 MHz Avance III HD spectrometer (Bruker BioSpin AG, Fällanden, Switzerland) equipped with a 5 mm cryogenic CP-TCI z-gradient probe at 25 °C (298.1 K).

A $^{13}$C-monitored psuedo-2D (zgig with interexperiment delay) spectrum followed by a $^{13}$C$^{1}$H HSQC (heteronuclear single quantum coherence; hsqcedetgpsisp2.3) spectrum was recorded for each reaction. The psuedo-2D consists of a series of 1D carbon spectra recorded every 5 min for a total of 200 spectra (total experiment time of 16 h 40 min). Each carbon spectrum (using inverse gated proton decoupling) contains 32 K data points, spectral width of 200 ppm, 32 scans with a 30° flip angle and relaxation delay of 2.1 s (total recording time of 81 s per spectrum). Proton chemical shifts were internally referenced to the residual water signal (4.75 ppm at 25 °C/298.1 K) and carbon chemical shifts were indirectly referenced to DSS (2,2-dimethyl-2-silapentane-5-sulfonic acid) using a $^{13}$C/$^{1}$H frequency ratio of 0.251449530[52]. Signals were assigned based previously published assigments from Heyraud et al.[53], Li et al.[54], and Mathieu et al.[55]. The spectra were recorded, processed, and analyzed using TopSpin 3.6pl7 and TopSpin 4.0.7 software (Bruker BioSpin AG, Fällanden, Switzerland).

### Crystallization, data collection, and data processing for X-ray structures

*Ps*Alg7A (14 mg ml$^{-1}$), *Ps*Alg7A-Y223F (15 mg ml$^{-1}$), *Ps*Alg7C (7.5 mg ml$^{-1}$), *Ps*Alg7C-H124N (7.5 mg ml$^{-1}$) and *Ps*Alg7C-Y220F (7.5 mg ml$^{-1}$) in 10 mM Tris-HCl, 150 mM NaCl pH 7 were crystallized in 48-well MRC Maxi plates (Jena Bioscience) (see crystallization conditions in Supplementary Table 2). The crystals soaked with di-, tri-, tetra-, penta-, or hexa-mannuronic sodium salt (Carbosynth) by adding a few crystals to the drop that were then allowed to equilibrate for 1–24 h. The crystals were supplemented with PEG1500 for cryoprotection, and the crystals were cryocooled in liquid nitrogen. Data were collected at BioMAX[56] at the MAX IV Laboratory and ID30B[57] at the European Synchrotron Radiation Facility using MxCUBE3[58] and P13[59] and P14 at PETRA III using MxCUBE2[60]. The dataset were processed to 0.82–2.00 Å resolution, respectively using XDSapp[61], Xia2[62] autoPROC[63] or EDNA[64] (see Supplementary Table 2 for statistics) in space groups $P1$, $P12_11$, $P2_12_12_1$, or $C12_1$.

### Phasing and refinement of X-ray structures

The structure of *Ps*Alg7A was determined by molecular replacement with PHASER[65] from the Phenix package[66] using the closest homolog at that time from the Protein Data Bank (www.pdb.org)[26] as a template, which was the PL7 alginate lyase A1-II' from *Sphingomonas* sp. A1 (PDB ID 2CWS)[67] identified through PDB-BLAST[68] with a coverage around 65% and identity of around 28%. The initial structure was built with PHENIX.autobuild[69] and then refined with PHENIX.refine[70] and manual model rebuilding in Coot[71]. The other *Ps*Alg7A and *Ps*Alg7C structures were obtained similarly but using *Ps*Alg7A as the template. The sugar moiety conformations were analyzed with Privateer[72].

### Crystallization, data collection at room temperature, and data processing for neutron structures

*Ps*Alg7C (15 mg ml$^{-1}$) in 10 mM Tris-HCl, 150 mM NaCl pH 7 dissolved in $H_2O$ was crystallized in Linbro plates (Jens Bioscience) by mixing 12 μl protein with 6 μl 0.1 M Bis-Tris pH 5.5, 30% PEG3350 and 0.3 M NaCl dissolved in $D_2O$ and incubated with 200 μl 0.1 M Bis-Tris pH 5.5, 30% PEG3350 and 0.3 M NaCl dissolved in $D_2O$ in the reservoir. After 1-week, crystals appeared, and the buffer was then exchanged by removing 5 μl from the drop followed by the addition of 5 μl 0.1 M Bis-Tris pH 5.5, 30% PEG3350, and 0.3 M NaCl dissolved in $D_2O$ and incubation for 24 h. This was repeated 5 times. Hexa-mannuronic sodium salt (Carbosynth) was added by dropping a few crystals on the drop that were then allowed to equilibrate for one week. The crystals were mounted in thin-walled quartz capillaries (Hampton) and sealed with beeswax.

Neutron time-of-flight diffraction data were collected at room temperature on the MaNDi instrument at the SNS[73,74]. An incident neutron wavelength bandpass of 2–4 Å was used. For the *Ps*Alg7C, a total of seven diffraction images were collected with a Δφ of 10° and an average exposure of 24 h per frame. Following neutron diffraction data collection, an X-ray dataset was collected on the same crystal at room temperature on a microfocus rotating anode X-ray diffractometer. A total of 360 diffraction images were collected with a Δφ of 1.0° and an exposure of 7 s per frame.

For *Ps*Alg7C in complex with PentaM, a total of 11 diffraction images were collected with a Δφ of 10° and an average exposure of 36 h per frame. Following neutron diffraction data collection, an X-ray dataset was collected on the same crystal at room temperature on a microfocus rotating anode X-ray diffractometer. A total of 180 diffraction images were collected with a Δφ of 1.0° and an exposure of 30 s per frame.

The neutron datasets were reduced using the *Mantid* package[75] and integrated using three-dimensional profile fitting[76]. The data were wavelength normalized using *LAUENORM* from the *LAUEGEN* suite[77,78]. The X-ray data were indexed and integrated using *CrysAlis PRO* (Rigaku, Woodlands, Texas, USA) and scaled and merged with *AIMLESS* in the *CCP4* suite[79]. X-ray and neutron data collection statistics are presented in Supplementary Table 2.

### Phasing and refinement of neutron structures

The structures of *Ps*Alg7C were determined by molecular replacement with PHASER[65] from the Phenix package[66] using *Ps*Alg7C (PDB ID 8C3X) as the template. Joint X-ray/neutron refinement was performed using the Phenix software suite[66] and manual model rebuilding in Coot[71] (see Supplementary Table 3 for statistics).

### Molecular dynamics simulations

The starting structure for all molecular dynamics (MD) simulations conducted in this study was the crystal structure of *Ps*Alg7A-Y223F in complex with HexaM (PDB ID 7NCZ). The catalytic residue mutation (Y223F) was reverted using PyMOL (Schödinger). The simulations were performed under conditions of pH 5 and 200 mM NaCl, which represent the optimal conditions for in vitro enzymatic analysis[13]. All arginine and lysine residues were positively charged, while all aspartate and glutamate residues, as well as all carboxylate groups of the M moieties, were negatively charged. The protonation states of the histidine residues were chosen using the H++ server[80] and guided by experimental data. The hydroxyl group of the Y223 catalytic residue was considered to be deprotonated, as per the β-elimination mechanism proposed in the literature and in previous works on related enzymes[46,48]. The system was positioned at the center of a periodically repeated rectangular box (77.725 × 83.850 × 90.199 Å$^3$), with a minimum distance of 15 Å between the solute surface and the box edge. The box was solvated with 14859 TIP3P[81] water molecules and sodium and chlorine ions were added to mimic the salt concentration for optimal activity (200 mM). The protein was described using the Amber ff14SB force field[82], while the GLYCAM06 force filed[83] was used to describe the carbohydrate molecule. Atomic partial charges (RESP) of Y223 (negatively charged) were calculated at the HF/6-31 G* level of theory using Gaussian09[84]. The topology and coordinate files for the classical MD simulations were generated using the LEaP module of AmberTools21[85]. The simulations were performed using Amber20[85] with the CUDA version of the PMEMD module[86]. The solvated system was subjected to an energy minimization protocol, wherein the solvent was minimized first with 5000 steps of steepest descent minimization

and 5000 steps of conjugate gradient minimization, with positional restraints applied to all atoms of the protein and the ligand. Subsequently, the entire system was minimized with 15,000 steps of steepest descend and conjugate gradients (7500 each). The system was then gradually heated to 308 K in the NVT ensemble using the Berendsen thermostat, with a time constant of 1.0 ps for the coupling and 50 kcal $mol^{-1}$ $Å^{-2}$ positional restraints applied to the heavy atoms of the protein and the substrate. The restraints were gradually decreased to 5 kcal $mol^{-1}Å^{-2}$ over three 500 ps steps, followed by 1000 ps of NPT equilibration using the Berendsen thermostat and barostat to maintain the system at 308 K and 1 atm, ensuring density equilibration. Three replicas were run for 250 ns, taking 50 ns as equilibration and 200 ns as production (Supplementary fig. 15). The SHAKE algorithm[87] was used to constrain all bonds involving hydrogen atoms, and the time step was set to 2 fs. Production runs in the NPT ensemble were controlled by the Langevin thermostat and the Berendsen barostat.

### QM/MM MD simulations of the β-elimination reaction

QM/MM MD simulations were employed to investigate the reaction mechanism in a less computationally demanding manner. This method involves partitioning the system into Quantum Mechanics (QM) and Molecular Mechanics (MM) fragments, where the QM region was treated using Born-Oppenheimer Density Functional Theory (DFT) based MD simulation, while the MM region was treated using force-field strategy. A snapshot form the classical MD trajectory (Supplementary Fig. 15) was used as the starting point for the QM/MM MD simulations. A large QM region (112 atoms) was selected, including the sidechains of residues R82, Q127, K219 and Y223, the saccharide residues at the +1 and −1 subsites and part of the ones at the +2 and −2 subsites (Supplementary Fig. 17). The QM region was enclosed in a cell of size 17.63 × 17.68 × 23.39 $Å^3$, and the atoms at the QM-MM border were saturated with hydrogen atoms using the IMMOM approach[88]. CP2K v9.0[41,42] was used for the QM/MM MD simulations. The QM region was treated at the DFT (PBE) level, employing the dual basis set of Gaussian and plane-waves (GPW) formalism. The wave function was expanded using the Gaussian triple- ζ valence polarized (TZV2P) basis set, and the electron density was converged using the auxiliary plane wave basis set with a density cutoff of 330 Ry and GTH pseudopotentials[89]. After relaxation, the system was equilibrated for 7 ps. Subsequently, the On-the-fly Probability Enhanced Sampling (OPES) method[43] in its exploratory variant ($OPES_E$) was used to explore the Free Energy surface. All QM/MM MD simulations were performed in the NVT ensemble using a coupling constant of 10 fs and an integration time step of 0.5 fs. Two CVs were used to activate the chemical reaction (Fig. 7): the first CV (CV1) was taken as the distance of the scissile glycosidic bond (O4′–C4). The second CV (CV2) was taken as a linear combination of distances involving H5 during the reaction, with negative values indicating the absence of a bond and positive values indicating its presence in the reactant state. The time interval between two consecutive kernels was set to 50 fs. To ensure a better description of the transition state (TS) and prevent exploration of non-catalytic high-energy regions, we set the initial $OPES_E$ energy barrier to 30 kcal $mol^{-1}$. The simulation was stopped after two recrossing over the TS (Supplementary Fig. 19). The minimum energy path was determined using the MEPS software[90], and the TS was further refined using iso-committor analysis (Supplementary Fig. 20). Mulliken charges of the QM atoms were computed and averaged from the first five configurations of each MD trajectory (nTS = 50), ensuring that the system remains at the TS. In the case of reactant and product states, charges were computed and averaged from unbiased QM/MM MD simulations (nR = 2000, nP = 2000). The MD trajectories generated in the simulations were analyzed using VMD[91], and distances between atoms were calculated using the driver module of PLUMED[92]. Plots were generated using Matplotlib[93], and figures of molecular structures were rendered using PyMOL (Shrödinger).

### QM/MM conformational analysis of the sugar at the *+1* subsite

To mitigate any potential bias inherent in the classical runs, we employed QM/MM metadynamics simulation to investigate the conformational landscape of the subsite +1 sugar of the $ManAC_7$ substrate within the enzyme (Supplementary Fig. 16). The simulation was initiated using the previously mentioned relaxed QM/MM structure (refer to the QM parameters provided above). Collective variables based on Cremer-Pople puckering coordinates, specifically $q_x$, $q_y$, and $q_z$ divided by the amplitude Q, were utilized. Gaussian biasing functions were employed, with a deposition pace of 60 MD steps (30 fs), and width of 0.05 Å, 0.05 Å and 0.03 Å for $q_x$/Q, $q_y$/Q and $q_z$/Q, respectively. The height of the Gaussians varied from 0.4 kcal/mol at the beginning of the simulation to 0.1 kcal/mol at the end. A total of 6789 Gaussians were deposited, and the simulation was carried out for 203.65 ps. Coordinate files and other simulation data can be found in the Zenodo repository (https://doi.org/10.5281/zenodo.14536694).

### Structural analysis

Structural alignments were obtained using PyMOL v. 2.5.4 (Schrödinger, LLC, New York; also used for rendering structural models). Electrostatic maps were obtained with the APBS-PDB2PQR software suite (https://server.poissonboltzmann.org/) using APBS v. 3.4.1 and PDB2PQR v. 3.6.1[94]. Hydrophobicity plots were obtained using the color_h.py script in PyMOL v. 2.5.4 (Schrödinger) and colored according to the Eisenberg hydrophobicity scale[95]. ProBiS $H_2O$ was used to identify conserved water molecules[96]. LigPlot+ v.2.2[97] and PyMOL v. 2.5.4 (Schrödinger) were used to analyze hydrogen bonds.

### Reporting summary

Further information on research design is available in the Nature Portfolio Reporting Summary linked to this article.

## Data availability

The X-Ray structures of *Ps*Alg7A, *Ps*Alg7A-hexaM, *Ps*Alg7A-pentaM, *Ps*Alg7A-tetraM, *Ps*Alg7A-triM, *Ps*Alg7A-diM, *Ps*Alg7A-Y223F, *Ps*Alg7A-Y223F-hexaM, *Ps*Alg7A-Y223F-pentaM, *Ps*Alg7A-Y223F-tetraM, *Ps*Alg7A-Y223F-triM, *Ps*Alg7A-Y223F-diM, *Ps*Alg7C, *Ps*Alg7C-hexaM, *Ps*Alg7C-pentaM, *Ps*Alg7C-tetraM, *Ps*Alg7C-triM, *Ps*Alg7C-diM, *Ps*Alg7C-Y220F, *Ps*Alg7C-Y220F-hexaM, *Ps*Alg7C-Y220F-pentaM, *Ps*Alg7C-Y220F-diM, *Ps*Alg7C-H110N, *Ps*Alg7C-H110N-hexaM, *Ps*Alg7C-H110N-pentaM, *Ps*Alg7C-H110N-tertaM and *Ps*Alg7C-H110N-triM generated in this study are deposited in the RCSB PDB with accession codes 6YWF, 7P25, 7ORY, 7P90, 7OOF, 7PBF, 7NL3, 7NCZ, 7NPP, 7NY3, 7O6H, 7NM6, 8C3X, 8PC8, 8PC3, 8PCX, 8PED, 8PDT, 8C0M, 8BJO, 8BXZ, 8P6O, 8RBI, 8QMJ, 8QIZ, 8QLI and 8R43, respectively. Joint X-ray and neutron diffraction structures of *Ps*Alg7C and *Ps*Alg7C-pentaM generated in this study are deposited in the RCSB PDB with accession codes 9G98 and 9G99, respectively. Data files of the classical MD simulation and QM/MM OPES simulations generated in this study are deposited in Zenodo [https://doi.org/10.5281/zenodo.14536694]. Other data are available from the corresponding authors upon request. Source data are provided with this paper.

## References

1. Aarstad, O. A., Tøndervik, A., Sletta, H. & Skjåk-Bræk, G. Alginate sequencing: an analysis of block distribution in alginates using specific alginate degrading enzymes. *Biomacromolecules* **13**, 106–116 (2012).
2. Kloareg, B. & Quatrano, R. S. Structure of the cell walls of marine algae and ecophysiological functions of the matrix polysaccharides. *Oceanogr. Mar. Biol. Annu. Rev.* **26**, 259–315 (1988).
3. Ertesvåg, H. Alginate-modifying enzymes: biological roles and biotechnological uses. *Front. Microbiol.* **6**, 523 (2015).

4. Nøkling-Eide, K. et al. Acid preservation of cultivated brown algae *Saccharina latissima* and *Alaria esculenta* and characterization of extracted alginate and cellulose. *Algal Res.* **71**, 103057 (2023).
5. Lu, S., Na, K., Wei, J., Zhang, L. & Guo, X. Alginate oligosaccharides: the structure-function relationships and the directional preparation for application. *Carbohydr. Polym.* **284**, 119225 (2022).
6. Varaprasad, K., Jayaramudu, T., Kanikireddy, V., Toro, C. & Sadiku, E. R. Alginate-based composite materials for wound dressing application: a mini review. *Carbohydr. Polym.* **236**, 116025 (2020).
7. Rønne, M. E., Madsen, M., Tandrup, T., Wilkens, C. & Svensson, B. Gut bacterial alginate degrading enzymes. *Essays Biochem.* **67**, 387–398 (2023).
8. Precedence Research, Alginate Market Size, Share, and Trends 2024–2034. https://www.precedenceresearch.com/alginate-market (Accessed Feb, 2025) (2024).
9. Puscaselu, R. G., Lobiuc, A., Dimian, M. & Covasa, M. Alginate: from food industry to biomedical applications and management of metabolic disorders. *Polymers* **12**, 2417 (2020).
10. Drula, E. et al. The carbohydrate-active enzyme database: functions and literature. *Nucleic Acids Res.* **50**, D571–D577 (2021).
11. Jouanneau, D. et al. Structure–function analysis of a new PL17 oligoalginate lyase from the marine bacterium *Zobellia galactanivorans* DsijT. *Glycobiology* **31**, 1364–1377 (2021).
12. Thomas, F. et al. Comparative characterization of two marine alginate lyases from *Zobellia galactanivorans* reveals distinct modes of action and exquisite adaptation to their natural substrate. *J. Biol. Chem.* **288**, 23021–23037 (2013).
13. Pilgaard, B., Vuillemin, M., Holck, J., Wilkens, C. & Meyer, A. S. Specificities and synergistic actions of novel PL8 and PL7 alginate lyases from the marine fungus *Paradendryphiella salina*. *J. Fungi* **7**, 80 (2021).
14. Petersen, A. B. et al. Mannuronate C-5 epimerases and their use in alginate modification. *Essays Biochem.* **67**, 615–627 (2023).
15. Xu, F., Wang, P., Zhang, Y. Z. & Chen, X. L. Diversity of three-dimensional structures and catalytic mechanisms of alginate lyases. *Appl. Environ. Microbiol.* **84**, e02040-17 (2018).
16. Gacesa, P. Alginate-modyfing enzymes. A proposed unified mechanism of action for the lyases and epimerases. *FEBS Lett.* **212**, 199–202 (1987).
17. Qin, H. M. et al. Structural basis for controlling the enzymatic properties of polymannuronate preferred alginate lyase FlAlyA from the PL-7 family. *ChemComm* **54**, 555–558 (2018).
18. Shaya, D. et al. Characterization of chondroitin sulfate lyase ABC from *Bacteroides thetaiotaomicron* WAL2926. *Biochem* **47**, 6650–6661 (2008).
19. Dong, S. et al. Molecular insight into the role of the N-terminal extension in the maturation, substrate recognition, and catalysis of a bacterial alginate lyase from polysaccharide lyase family 18. *J. Biol. Chem.* **289**, 29558–29569 (2014).
20. Dong, F. et al. Alginate lyase Aly36B is a new bacterial member of the polysaccharide lyase family 36 and catalyzes by a novel mechanism with lysine as both the catalytic base and catalytic acid. *J. Mol. Biol.* **431**, 4897–4009 (2019).
21. Xu, F. et al. Structural and molecular basis for the substrate positioning mechanism of a new PL7 subfamily alginate lyase from the Arctic. *J. Biol. Chem.* **295**, 16380–16392 (2020).
22. Ogura, K., Yamasaki, M., Mikami, B., Hashimoto, W. & Murata, K. Substrate recognition by family 7 alginate lyase from *Sphingomonas* sp. A1. *J. Mol. Biol.* **380**, 373–385 (2008).
23. Vuillemin, M. et al. Glucuronan lyases from family PL7 use a Tyr/Tyr syn β-elimination catalytic mechanism for glucuronan breakdown. *ChemComm* **60**, 440–443 (2024).
24. Zhang, K. et al. Determination of oligosaccharide product distributions of PL7 alginate lyases by their structural elements. *Commun. Biol.* **5**, 782 (2022).
25. Pilgaard, B. et al. Proteomic enzyme analysis of the marine fungus *Paradendryphiella salina* reveals alginate lyase as a minimal adaptation strategy for brown algae degradation. *Sci. Rep.* **9**, 12338 (2019).
26. Berman, H. M. et al. The Protein Data Bank. *Nucleic Acids Res.* **28**, 235–242 (2000).
27. Holm, L. Dali server: structural unification of protein families. *Nucleic Acids Res.* **50**, W210–W215 (2022).
28. Davies, G. J., Wilson, K. S. & Henrissat, B. Nomenclature for sugar-binding subsite in glycosyl hydrolases. *Biochem J.* **559**, 557–559 (1997).
29. Davies, G. J., Planas, A. & Rovira, C. Conformational analyses of the reaction coordinate of glycosidases. *Acc. Chem. Res.* **45**, 308–316 (2012).
30. Wilkens, C. et al. Plant α-glucan phosphatases SEX4 and LSF2 display different affinity for amylopectin and amylose. *FEBS Lett.* **590**, 118–128 (2016).
31. Wilkens, C. et al. Asp271 is critical for substrate interaction with the surface binding site in β-agarase a from *Zobellia galactanivorans*. *Proteins: Struct. Funct. Bioinf.* **87**, 34–40 (2019).
32. Wilkens, C., Cuesta-Seijo, J. A., Palcic, M. & Svensson, B. Selectivity of the surface binding site (SBS) on barley starch synthase I. *Biologia* **69**, 1118–1121 (2014).
33. Harris, T. K. & Turner, G. J. Structural basis of perturbed pKa values of catalytic groups in enzyme active sites. *IUBMB Life* **53**, 85–98 (2002).
34. Da Costa, M. et al. Structure-function relationships in NDP-sugar active SDR enzymes: fingerprints for functional annotation and enzyme engineering. *Biotech. Adv.* **48**, 107705 (2021).
35. Liu, Y. et al. Mechanistic roles of tyrosine 149 and serine 124 in UDP-galactose 4-epimerase from *Escherichia coli*. *Biochem* **36**, 10675–10684 (1997).
36. Savino, S. et al. Deciphering the enzymatic mechanism of sugar ring contraction in UDP-apiose biosynthesis. *Nat. Catal.* **2**, 1115–1123 (2019).
37. Watanabe, A. et al. Reaction mechanism of alanine racemase from *Bacillus stearothermophilus*: X-ray crystallographic studies of the enzyme bound with N-(5′-phosphopyridoxyl)alanine. *J. Biol. Chem.* **277**, 19166–19172 (2002).
38. Barducci, A., Bonomi, M. & Parrinello, M. Metadynamics. *Wiley Interdiscip. Rev. Comput Mol. Sci.* **1**, 826–843 (2011).
39. Ardevol, A. & Rovira, C. Reaction mechanisms in carbohydrate-active enzymes: glycoside hydrolases and glycosyltransferases. Insights from ab Initio quantum mechanics/molecular mechanics dynamic simulations. *J. Am. Chem. Soc.* **137**, 7525–7547 (2015).
40. Iglesias-Fernández, J., Raich, L., Ardèvol, A. & Rovira, C. The complete conformational free energy landscape of β-xylose reveals a two-fold catalytic itinerary for β-xylanases. *Chem. Sci.* **6**, 1167–1177 (2015).
41. Laino, T., Mohamed, F., Laio, A. & Parrinello, M. An efficient real space multigrid QM/MM electrostatic coupling. *J. Chem. Theory Comput.* **1**, 1176–1184 (2005).
42. Hutter, J., Iannuzzi, M., Schiffmann, F. & Vandevondele, J. Cp2k: atomistic simulations of condensed matter systems. *Wiley Interdiscip. Rev. Comput. Mol. Sci.* **4**, 15–25 (2014).
43. Invernizzi, M. & Parrinello, M. Rethinking metadynamics: from bias potentials to probability distributions. *J. Phys. Chem. Lett.* **11**, 2731–2736 (2020).
44. Invernizzi, M., Piaggi, P. M. & Parrinello, M. Unified approach to enhanced sampling. *Phys. Rev. X* **10**, 041034 (2020).
45. Raucci, U., Rizzi, V. & Parrinello, M. Discover, sample, and refine: exploring chemistry with enhanced sampling techniques. *J. Phys. Chem. Lett.* **13**, 1424–1430 (2022).
46. Lombard, V. et al. A hierarchical classification of polysaccharide lyases for glycogenomics. *Biochem J.* **432**, 437–444 (2010).

47. Rye, C. S. & Withers, S. G. Elucidation of the mechanism of polysaccharide cleavage by chondroitin AC lyase from *Flavobacterium heparinum*. *J. Am. Chem. Soc.* **124**, 9756–9767 (2002).
48. Zheng, M. & Xu, D. Catalytic mechanism of hyaluronate lyase from *Spectrococcus pneumonia*: quantum mechanical/molecular mechanical and density functional theory studies. *J. Phys. Chem. B* **117**, 10161–10172 (2013).
49. Charnock, S. J., Brown, I. E., Turkenburg, J. P., Black, G. W. & Davies, G. J. Convergent evolution sheds light on the anti-β-elimination mechanism common to family 1 and 10 polysaccharide lyases. *Proc. Natl. Acad. Sci. USA* **99**, 12067–12072 (2002).
50. Gimmestad, M. et al. The Pseudomonas fluorescens AlgG protein, but not its mannuronan C-5-epimerase activity, is needed for alginate polymer formation. *J. Bacteriol.* **185**, 3515–3523 (2003).
51. Ertesvåg, H. & Skjåk-Bræk, G. Modification of alginate using mannuronan C-5-epimerases. In *Carbohydrate Biotechnology Protocols. Methods in Biotechnology* (ed. Bucke, C.) Vol. 10, 77–78 (Humana Press, 1999).
52. Wishart, D. S. et al. $^{1}$H, $^{13}$C and $^{15}$N chemical shift referencing in biomolecular NMR. *J. Biomol. NMR* **6**, 135–140 (1995).
53. Heyraud, A. et al. NMR spectroscopy analysis of oligoguluronates and oligomannuronates prepared by acid or enzymatic hydrolysis of homopolymeric blocks of alginic acid application to the determination of the substrate specificity of *Haliotis tuberculata* alginate lyase. *Carbohydr. Res.* **289**, 11–23 (1996).
54. Li, L., Jiang, X., Guan, H. & Wang, P. Preparation, purification and characterization of alginate oligosaccharides degraded by alginate lyase from *Pseudomonas* sp. HZJ 216. *Carbohydr. Res.* **346**, 794–800 (2011).
55. Mathieu, S., Henrissat, B., Labre, F., Skjåk-Bræk, G. & Helbert, W. Functional exploration of the polysaccharide lyase family PL6. *PLoS ONE* **11**, e0159415 (2016).
56. Ursby, T. et al. BioMAX the first macromolecular crystallography beamline at MAX IV Laboratory. *J. Synchrotron Radiat.* **27**, 1415–1429 (2020).
57. McCarthy, A. A. et al. ID30B – a versatile beamline for macromolecular crystallography experiments at the ESRF. *J. Synchrotron Radiat.* **25**, 1249–1260 (2018).
58. Mueller, U. et al. MXCuBE3: a new era of MX-beamline control begins. *Synchrotron. Radiat. N.* **30**, 22–27 (2017).
59. Cianci, M. et al. P13, the EMBL macromolecular crystallography beamline at the low-emittance PETRA III ring for high- and low-energy phasing with variable beam focusing. *J. Synchrotron Radiat.* **24**, 323–332 (2017).
60. Oscarsson, M. et al. MXCuBE2: the dawn of MXCuBE collaboration. *J. Synchrotron Radiat.* **26**, 393–405 (2019).
61. Sparta, K. M., Krug, M., Heinemann, U., Mueller, U. & Weiss, M. S. Xdsapp2.0. *J. Appl. Crystallogr.* **49**, 1085–1092 (2016).
62. Winter, G. Xia2: An expert system for macromolecular crystallography data reduction. *J. Appl. Crystallogr.* **43**, 186–190 (2010).
63. Vonrhein, C. et al. Data processing and analysis with the autoPROC toolbox. *Acta Crystallogr. D. Biol. Crystallogr.* **67**, 293–302 (2011).
64. Incardona, M. F. et al. EDNA: a framework for plugin-based applications applied to X-ray experiment online data analysis. *J. Synchrotron Radiat.* **16**, 872–879 (2009).
65. McCoy, A. J. et al. Phaser crystallographic software. *J. Appl. Crystallogr.* **40**, 658–674 (2007).
66. Liebschner, D. et al. Macromolecular structure determination using X-rays, neutrons and electrons: recent developments in Phenix. *Acta Crystallogr. D. Struct. Biol.* **75**, 861–877 (2019).
67. Yamasaki, M., Ogura, K., Hashimoto, W., Mikami, B. & Murata, K. A structural basis for depolymerization of alginate by polysaccharide lyase family-7. *J. Mol. Biol.* **352**, 11–21 (2005).
68. Altschul, S. F. et al. Gapped BLAST and PSI-BLAST:a new generation of protein database search programs. *Nucleic Acids Res.* **25**, 3389–3402 (1997).
69. Terwilliger, T. C. et al. Iterative model building, structure refinement and density modification with the PHENIX AutoBuild wizard. *Acta Crystallogr. D. Biol. Crystallogr.* **64**, 61–69 (2007).
70. Afonine, P. V. et al. Towards automated crystallographic structure refinement with phenix.refine. *Acta Crystallogr. D. Biol. Crystallogr.* **68**, 352–367 (2012).
71. Emsley, P., Lohkamp, B., Scott, W. G. & Cowtan, K. Features and development of Coot. *Acta Crystallogr. D. Biol. Crystallogr.* **66**, 486–501 (2010).
72. Agirre, J. et al. Privateer: software for the conformational validation of carbohydrate structures. *Nat. Struct. Mol. Biol.* **22**, 833–834 (2015).
73. Meilleur, F., Coates, L., Cuneo, M. J., Kovalevsky, A. & Myles, D. A. A. The neutron macromolecular crystallography instruments at Oak Ridge National Laboratory: advances, challenges, and opportunities. *Crystals* **8**, 388 (2018).
74. Coates, L. & Sullivan, B. The macromolecular neutron diffractometer at the spallation neutron source. In *Methods in Enzymology* (ed. Moody, P. C. E.) Vol. 634, 87–99 (Academic Press Inc., 2020).
75. Arnold, O. et al. Mantid—Data analysis and visualization package for neutron scattering and u SR experiments. *Nucl. Instrum. Methods Phys. Res. A* **764**, 156–166 (2014).
76. Sullivan, B. et al. Improving the accuracy and resolution of neutron crystallographic data by three-dimensional profile fitting of Bragg peaks in reciprocal space. *Acta Crystallogr. D. Struct. Biol.* **74**, 1085–1095 (2018).
77. Artz, S. et al. The Daresbury Laboratory Laue software suite. *Acta Crystallogr. A* **52**, C50–C50 (1996).
78. Campbell, J. W., Hao, Q., Harding, M. M., Nguti, N. D. & Wilkinson, C. LAUEGEN version 6.0 and INTLDM. *J. Appl. Crystallogr.* **31**, 496–502 (1998).
79. Evans, P. R. & Murshudov, G. N. How good are my data and what is the resolution? *Acta Crystallogr. D. Biol. Crystallogr.* **69**, 1204–1214 (2013).
80. Anandakrishnan, R., Aguilar, B. & Onufriev, A. V. H++ 3.0: automating pK prediction and the preparation of biomolecular structures for atomistic molecular modeling and simulations. *Nucleic Acids Res.* **40**, 537–541 (2012).
81. Jorgensen, W. L., Chandrasekhar, J., Madura, J. D., Impey, R. W. & Klein, M. L. Comparison of simple potential functions for simulating liquid water. *J. Chem. Phys.* **79**, 926 (1983).
82. Maier, J. A. et al. ff14SB: improving the accuracy of protein side chain and backbone parameters from ff99SB. *J. Chem. Theory Comput.* **11**, 3696–3713 (2015).
83. Kirschner, K. N. et al. GLYCAM06: a generalizable biomolecular force field. carbohydrates. *J. Comput. Chem.* **29**, 622–655 (2008).
84. Frisch, M. J. et al. *Gaussian 09, Revision B.01* https://gaussian.com/g09citation/ (Wallingford CT, 2009).
85. Case, D. A., Aktulga, H. M., Belfron, K., Ben-Shalom, I. Y. & Brozell, S. R. *Amber 2021* (Amber, University of California, San Francisco, 2021).
86. Götz, A. W. et al. Routine microsecond molecular dynamics simulations with AMBER on GPUs. 1. generalized born. *J. Chem. Theory Comput.* **8**, 1542–1555 (2012).
87. Ryckaert, J.-P., Ciccotti, G. & Berendsen, H. J. C. Numerical integration of the Cartesian equations of motion of a system with constraints: molecular dynamics of n-Alkanes. *J. Comput. Phys.* **23**, 327–341 (1977).
88. Woo, T. K., Cavallo, L. & Ziegler, T. Implementation of the IMOMM methodology for performing combined QM/MM molecular

dynamics simulations and frequency calculations. *Theor. Chem. Acc.* **100**, 307–319 (1998).
89. Goedecker, S., Teter, M. & Hutter, J. Separable dual-Space Gaussian pseudopotentials. *Phys. Rev. B Condens Matter* **54**, 1703–1710 (1996).
90. Marcos-Alcalde, I., López-Viñas, E. & Gómez-Puertas, P. MEPSAnd: minimum energy path surface analysis over n-dimensional surfaces. *Bioinformatics* **36**, 956–958 (2020).
91. Humphrey, W., Dalke, A. & Schulten, K. VMD: visual molecular dynamics. *J. Mol. Graph* **14**, 33–38 (1996).
92. The PLUMED consortium. Promoting transparency and reproducibility in enhanced molecular simulations. *Nat. Methods* **16**, 670–673 (2019).
93. Hutter, J. D. Matplotlib: a 2D graphics environment. *Comput. Sci. Eng.* **9**, 90–95 (2007).
94. Jurrus, E. et al. Improvements to the APBS biomolecular solvation software suite. *Protein Sci.* **27**, 112–128 (2018).
95. Eisenberg, D., Schwarz, E., Komaromy, M. & Wall, R. Analysis of membrane and surface protein sequences with the hydrophobic moment plot. *J. Mol. Biol.* **179**, 125–142 (1984).
96. Jukič, M., Konc, J., Gobec, S. & Janežič, D. Identification of conserved water sites in protein structures for drug design. *J. Chem. Inf. Model* **57**, 3094–3103 (2017).
97. Laskowski, R. A. & Swindells, M. B. LigPlot+: multiple ligand-protein interaction diagrams for drug discovery. *J. Chem. Inf. Model* **51**, 2778–2786 (2011).

## Acknowledgements

This study was funded by the European Commission JPI Cofund Blue BioEconomy via the MARIKAT project (9082-00021B), the Research Council of Norway (RCN) via the AlgModE project (315385), the Independent Research Fund Denmark via the DSMADE project (DFF170746) and by the Department of Biotechnology and Biomedicine (DTU Bioengineering), Enzyme Discovery & Engineering Program, Technical University of Denmark, the Spanish Ministry of Science and Innovation (MICINN/AEI/FEDER, UE, PID2020-118893GB-100, to C.R.), the Spanish Structures of Excellence María de Maeztu (CEX2021-001202-M, to C.R.), the Agency for Management of University and Research Grants of Catalonia (AGAUR, 2021-SGR-00680, to C.R.) and the European Research Council (ERC-2020-SyG-951231 "Carbocentre", to C.R.). J.P.R. was supported by MICINN (FPI fellowship PRE2021-097898). F.F. and D.H.W. were supported by The Novo Nordisk Foundation through grant number NNF10CC1016517 to the Novo Nordisk Foundation Center for Biosustainability at the Technical University of Denmark, which also supported the collection of some of the crystallographic data. We thank the Danish Agency for Science, Technology, and Innovation for funding the instrument center DanScatt, which supported our usage of beam time at the synchrotrons. The authors acknowledge MAX IV Laboratory for time on Beamline BioMAX under Proposal MX20190334 and MX20200120. Research conducted at MAX IV, a Swedish national user facility, is supported by the Swedish Research council under contract 2018-07152, the Swedish Governmental Agency for Innovation Systems under contract 2018-04969, and Formas under contract 2019-02496. The authors acknowledge synchrotron beamline P13 and P14 operated by EMBL Hamburg at the PETRA III storage ring (DESY, Hamburg, Germany), on which data were also collected. The authors acknowledge the European Synchrotron Radiation Facility for the provision of beam time on ID30B operated by EMBL Grenoble. The authors acknowledge the Spallation Neutron Source, a DOE Office of Science User Facility operated by the Oak Ridge National Laboratory for the provision of beam time. R.C.N. is also acknowledged for funding the Norwegian NMR Platform (226244), SBP-N (294946), and the Carlsberg Foundation for funding the Mosquito crystallization robot, which was used for obtaining some of the protein crystals. The authors are grateful for the technical assistance provided by the support of the MareNostrum IV and CTE-Power supercomputers of the Barcelona Supercomputing Center (BSC-CNS), within the Red Española de Supercomputación (RES).

## Author contributions

C.W. and C.R. conceived and designed the study with input from A.S.M.; M.V., B.P., L.J.K., C.L.-H. performed all molecular biology and biochemical experiments with help from F.L.A. and C.W.; C.W. and F.F. performed all the X-ray crystallography experiments with the help from D.H.W., C.W., J.P.M., and F.M. performed the neutron crystallography experiments; J.P.R.-F. performed the computational experiments. C.W. and C.R. wrote the article, with contributions from all authors. All authors read and approved the final manuscript.

## Competing interests

The authors declare no competing interests.

## Additional information

**Supplementary information** The online version contains supplementary material available at https://doi.org/10.1038/s41467-025-56754-5.

**Correspondence** and requests for materials should be addressed to Carme Rovira or Casper Wilkens.

**Peer review information** *Nature Communications* thanks Giulia Palermo and the other, anonymous, reviewers for their contribution to the peer review of this work. A peer review file is available.